Progress in Organic Coatings 222 (2027) 110710

Contents lists available at ScienceDirect

Progress in Organic Coatings

journal homepage: www.elsevier.com/locate/porgcoat

D-optimal optimization of photothermal polyurethane hybrid coatings for durable low ice adhesion performance

Mohammad Bakhtiari [a,*], Gelareh Momen [b], Reza Jafari [a]

[a] Department of Applied Sciences, University of Quebec in Chicoutimi (UQAC), 555, boul. de l'Université, Chicoutimi, Quebec, G7H 2B1, Canada
[b] Department of Aerospace Engineering, École de Technologie Supérieure (ÉTS), Montreal, Quebec, H3C 1K3, Canada

ARTICLE INFO

Keywords:
Icephobic Coatings
Photothermal Nanoparticles
Self-Lubricating
Polyurethane
Design of Experiments (DoE)
Anti-Icing
De-Icing Performance
Response Surface Methodology

ABSTRACT

This study presents a statistical optimization of polyurethane (PU) hybrid coatings designed to reconcile the trade-off between mechanical durability, low ice adhesion, and invistigate photothermal properties of coating. A D-optimal experimental design based on Response Surface Methodology (RSM), to ensure statistical validity, was employed, comprising 18 distinct runs. This approach was used to investigate the dominant factors governing key coating characteristics, including surface wettability, roughness, mechanical and photothermal properties, ice formation temperature, and ice adhesion strength (IAS). These responses were evaluated by comparing two different architectures of amphiphilic PEG/PDMS copolymers (linear vs. graft) and adjusting the concentration of silicone oil-coated Fe_3O_4 nanoparticles. The RSM analysis revealed that copolymer content is the dominant factor driving wettability and passive anti-icing behavior, with the linear triblock PEG-b-PDMS-b-PEG copolymer (DBE-C25, 40% siloxane content) demonstrating superior surface segregation compared to the graft poly(dimethylsiloxane-*graft*-PEG) copolymer (CMS-626, 35% siloxane content) and nanoparticle content was identified as the dominant factor for photothermal response and surface roughness. A significant Copolymer × Nanoparticle interaction (AB) was identified for mechanical properties. The copolymer phase buffers the rigid Fe_3O_4 particles within the PU matrix and mitigates embrittlement. The same AB interaction was not significant for ice nucleation temperature, indicating that the two additives suppress nucleation through independent mechanisms.

To validate synergistic de-icing potential, we developed a dynamic photothermal-inclined plane test. The optimized formulation (7.5 wt% linear copolymer, 5 wt% nanoparticles) successfully reconciled the trade-off between mechanical durability, ultra-low ice adhesion, and rapid photothermal response. It maintained robust mechanical integrity while delivering an ultra-low IAS of 17 ± 7 kPa in push-off and 78.6 ± 17.5 kPa in centrifugal tests and a rapid thermal response of 8.6 °C/min. This synergistic combination enabled the rapid shedding of 3 mm ice layers in just 12 ± 3 min at −5 °C under 1 sun irradiation. Furthermore, a 50-cycle icing/de-icing durability analysis at −10 °C confirmed the coating's long-term operational stability. The optimized hybrid degraded at a negligible rate of 0.22 kPa/cycle and sustained a 50-cycle mean IAS of 21 kPa. These results demonstrate that the optimized hybrid coating retains low ice adhesion over 50 icing/deicing cycles under the tested conditions.

1. Introduction

The critical challenges and substantial costs associated with icing worldwide, particularly in sectors such as aviation, energy, and transportation, are the primary drivers of the growing global emphasis on energy-efficient and sustainable surface technologies [1–5]. Nordic countries possess significant wind energy potential during winter due to higher wind speeds and increased air density, which enhance power generation efficiency [6]. However, these advantages are often compromised by ice accretion on turbine blades. Ice accumulation can reduce the aerodynamic efficiency of the blades by 20–50%, leading to substantial energy losses and significant economic costs. Additionally, these harsh conditions introduce complex challenges, such as increased mechanical fatigue on the turbine structure and safety risks from shedding ice [6,7]. Traditional de-icing methods including thermal, mechanical and chemical are highly problematic due to their substantial energy consumption, low efficiency, high cost, and the use of environmentally hazardous materials and volatile organic compounds. In

* Corresponding author.
E-mail address: mbakhtiari@etu.uqac.ca (M. Bakhtiari).

https://doi.org/10.1016/j.porgcoat.2026.110710
Received 21 June 2026; Received in revised form 4 October 2026; Accepted 21 October 2026
Available online 28 October 2026
0300-9440/© 2026 The Authors. Published by Elsevier B.V. This is an open access article under the CC BY-NC-ND license (http://creativecommons.org/licenses/by-nc-nd/4.0/).

response, recent research has focused on developing coatings that can delay ice formation passively while minimizing energy consumption during ice removal [8–10]. Solar radiation, a clean and renewable energy source, is converted into thermal energy by photothermal de-icing, which is a scalable and energy-efficient method [11,12].

Photothermal coating systems utilize nanoparticles that absorb light and convert it into thermal energy to actively melt the ice interface, creating a lubricating layer for facile removal by natural forces (e.g., wind/gravity). Wu et al. [13] developed a composite of candle soot with silica shells and polydimethylsiloxane (PDMS), resulting in a surface temperature increase of 53 °C under 1 sun illumination, enabling ice melting within 300 s. However, the material cannot reach its full potential because these structures usually have issues like poor mechanical durability under abrasion and not functioning effectively at night or in low light. It is challenging to use these materials to large-scale engineering projects with complex curved surfaces because most recent studies have concentrated on small-scale laboratory tests on rigid substrates [14,15].

Polymer-based systems, notably polyurethane (PU), offer substantial advantages for multifunctional surface design due to their exceptional properties, including durability, toughness, elasticity, high hardness, strong adhesion, and inherent resistance to wear, chemicals, and weathering. For instance, Li et al. [16] created a superhydrophobic anti-icing coating using thermoplastic polyurethane (TPU) synergistically enhanced by polydimethylsiloxane (PDMS)-modified multi-walled carbon nanotubes (MWCNTs) and stearic acid-modified zinc oxide, which extended the water droplet freezing time by 970% (to 612 s at −15 °C) compared to pure TPU and maintained superhydrophobicity after 30 abrasion cycles. Similarly, Paleo et al. [17] developed a single-wall carbon nanotube (SWCNT) and TPU composite. This made it about 25 times stronger and 250 times tougher than pure SWCNT buckypaper. Therefore, using polyurethane matrices reinforced with functional nanofillers is clearly effective for improving mechanical durability, photothermal conversion efficiency, and ice adhesion reduction [16,17]. This approach helps to replace energy-intensive de-icing methods with passive/active dual-mode systems that maintain robustness under mechanical stress. However, these superhydrophobic photothermal architectures often face problems such as the degradation of surface micro-nano hierarchical structures under long-term mechanical wear and the loss of icephobicity in extremely low-temperature and high-humidity conditions where vapor condensation leads to mechanical interlocking [18].

Our previous study [19] demonstrated the successful development of polyurethane coatings incorporating PEG/PDMS amphiphilic copolymers, resulting in enhanced icephobic performance. These coatings reduced the ice adhesion strength to less than 50 kPa by the self-lubricating properties of PEG/PDMS copolymers. These properties have attracted considerable attention due to their ability to form hydrophilic surface layers that induce non-frozen interfacial water, thereby reducing ice adhesion strength. However, these structures often face problems such as the trade-off between mechanical durability and low ice adhesion strength in soft coatings. In this article, we discuss the development and optimization of dual-function polyurethane (PU) coatings that incorporate PEG/PDMS copolymer for self-lubrication along with Fe_3O_4 nanoparticles for photothermal heating. Nonetheless, the concurrent impact of these two factors on anti-icing efficacy remains ambiguous. Optimizing copolymer and nanoparticle concentrations at the same time is a difficult undertaking that requires a systematic approach.

This investigation focuses on the integration and optimization of the most effective components identified in our previous works [19,20], combining PEG/PDMS copolymers for self-lubrication with functionalized photothermal nanoparticles within a polyurethane matrix. This study presents a novel multifunctional anti−/de-icing coating that integrates PEG/PDMS-based self-lubrication with photothermal nanoparticles within a polyurethane matrix. Unlike previous studies that have investigated these functionalities separately, this work systematically explores their synergistic interaction using a D-optimal Response Surface Methodology (RSM) design. Two different PEG/PDMS copolymers (626 and C25) are used to study the integration of photothermal nanoparticles in a polyurethane matrix. The functional components were incorporated directly into the PU formulation, followed by application and curing, without a separate lubricant-infusion step. Design-Expert® software was used to investigate three primary factors: copolymer type, copolymer content, and nanoparticle loading. Responses such as de-icing time, mechanical durability, and ice adhesion strength are monitored to quantify the synergistic effects of these components. This approach establishes quantitative links between the controllable formulation variables (copolymer architecture, copolymer content, nanoparticle loading) and the six measured coating responses (wettability, roughness, modulus, photothermal temperature rise, ice formation temperature, ice adhesion strength) that facilitate the development of durable and energy-efficient anti/de-icing coatings. These relationships are further supported by complementary performance assessments, including push-off and centrifugal ice adhesion measurements, repeated icing/de-icing cycles, and outdoor observations of the resulting coatings.

2. Materials and methods

2.1. Materials

The silicone oil-coated Fe_3O_4 nanoparticles (99% purity) were supplied by US Nano. These nanoparticles had an average size of 20–30 nm and a specific surface area of 40–60 m^2/g. For the amphiphilic copolymer, CMS-626 (65% non-siloxane, graft topology) and DBE-C25 (60% non-siloxane, linear topology) were used, both supplied by Gelest Inc.. The coating matrix consisted of SETALUX® 1909 BA, an acrylic polyol supplied by Alnex Chemical Company (5 wt% hydroxyl content, 75% solid content). The hardener was Tolonate™ HDB 75BX (16.5% NCO content), obtained from Vencorex. To adjust the viscosity, n-Butyl acetate (99%) from Thermo Fisher Scientific were used. Finally, Aluminum alloy (A6061) substrates underwent a rigorous cleaning process consisting of a distilled water rinse followed by triple-washing with acetone.

2.2. Design of experiments

This study employed RSM to enhance the anti-icing efficacy of polyurethane hybrid coatings. Throughout this paper, hybrid refers to a coating that combines two complementary icephobic mechanisms in one formulation: passive self-lubrication via PEG/PDMS amphiphilic copolymers, and active solar-driven photothermal heating via silicone-oil-coated Fe_3O_4 nanoparticles. A D-optimal design was selected using Design-Expert® software (version 12.0.3.0) to minimize the determinant of the variance-covariance matrix, giving the best parameter precision for the samples. The experimental framework focused on three principal variables as delineated in Table 1. The study included 18 randomized runs to guarantee statistical validity, as outlined in Table 2. Each run's stoichiometry was determined by using a constant mass for the polyol part and adjusting the additive masses dynamically to meet the specified weight percentages.

2.3. Preparation of hybrid coatings

The fabrication of the hybrid coatings involved the sequential incorporation of photothermal nanoparticles and amphiphilic PEG/PDMS copolymers into a polyurethane host matrix. First, the nanoparticles were introduced into the polyol/solvent component (amount as listed for each run in Table 2) by ultrasonication (100 Hz, 20 min) to prevent particle agglomeration. Thereafter, the PEG/PDMS copolymer (type and amount as listed for each run in Table 2) was incorporated into the suspension. The mixture underwent vigorous mechanical stirring for

Table 1
Experimental factors and levels used in the Design of Experiments.

Factor	Name	Units	Type	Minimum	Maximum	Levels
A	Copolymer Content	(%)	Numeric	0.00	15.00	–
B	Nanoparticle Content	(%)	Numeric	0.00	10.00	–
C	Copolymer Type	–	Categoric	DBE-C25	CMS-626	2

Table 2
Experimental design and formulation details. SIF refers to silicone oil coated Fe_3O_4. All formulations used 50.00 g of Polyol and 28.05 g of Hardener.

Run	Type	Sample name	Composition (%)		Weight (g)	
			Copolymer	SIF	Copolymer	SIF
1	626	S1	7.58	10.00	5.38	7.10
2		S2	0.00	0.00	0.00	0.00
3	C25	S3	15.00	10.00	11.71	7.81
4	626	S4	15.00	0.00	10.33	0.00
5		S5	0.00	3.50	0.00	2.13
6	626	S6	15.00	10.00	11.71	7.81
7	C25	S7	7.50	0.00	4.75	0.00
8	C25	S8	15.00	0.00	10.33	0.00
9	C25	S9	15.00	10.00	11.71	7.81
10	626	S10	5.25	0.00	3.25	0.00
11		S11	0.00	10.00	0.00	6.51
12		S12	0.00	10.00	0.00	6.51
13		S13	0.00	5.00	0.00	3.08
14	626	S14	15.00	5.05	10.99	3.70
15		S15	0.00	10.00	0.00	6.51
16	C25	S16	15.00	0.00	10.33	0.00
17	C25	S17	7.50	5.00	5.02	3.35
18	626	S18	7.35	4.85	4.90	3.24

60 min to ensure homogeneity prior to the addition of the curing agent. Once a homogeneous dispersion was achieved, the hardener was added. The final formulations were cast onto prepared substrates using a spin coater (Zehntner ZUA2000 universal applicator). To achieve thickness coatings, the spin coating speed was set to 50 rpm with a coating drop rate of 0.2 mL/s(wet thickness = 200 ± 15 μm). The coatings were allowed to cure in a controlled environment (25 °C) for one week, yielding a consistent dry thickness of 125 ± 8 μm.

The nominal VOC content of the uncured formulations was estimated from the mass of organic solvent introduced during preparation and the corresponding nominal formulation volume. Solvent mass fraction was additionally calculated relative to the total formulation mass. These values represent formulation-based estimates rather than experimentally measured VOC content or emissions.

2.4. Characterization

2.4.1. Surface roughness

Surface roughness was evaluated using a Profilm3D optical profilometer (Filmetrics®, USA). This instrument incorporates white light interferometry (WLI) to obtain surface profiles and roughness values with a resolution of 0.05 μm. The measurements were performed over an 800 × 800 μm area, and five randomly selected regions were analyzed per sample.

2.4.2. Wettability analysis

The wetting characteristics of the surfaces were evaluated using the sessile drop method on a Krüss DSA100 goniometer at 25 ± 0.5 °C. Static Water Contact Angle (WCA) measurements were obtained by depositing a 4 μL distilled water droplet on the coating, with the shape analyzed via ADVANCE software. For dynamic wettability, the sliding angle (SA) was determined using a tilting platform. A 35 μL droplet was subjected to an inclination rate of 60°/min, and the angle was recorded immediately prior to the onset of sliding. Additionally, Contact Angle Hysteresis (CAH) was determined by calculating the difference between the advancing and receding contact angles.

2.4.3. Photothermal properties

Photothermal performance was evaluated by exposing the coatings to a xenon lamp with an intensity of ~1 kW/m^2, simulating solar irradiation. The light source delivers light vertically; to achieve this, the setup utilizes UV-Enhanced Aluminum Zerodur Mirrors (250 nm–450 nm) from Thorlabs. This configuration directs a vertical column of light onto the surface, as illustrated in Fig. 1a. The spectral power distribution of the light source (SLS401) is presented in Fig. 1b. The experiment was conducted at room temperature to replicate typical environmental conditions. To monitor the surface temperature evolution, an infrared thermal camera (Optris Pi450i, Optris, Berlin, Germany) was employed. The camera, equipped with a 382 × 288 pixel uncooled microbolometer, was positioned 40 cm from the sample surface. Prior to data acquisition, the system was allowed to stabilize for 30 min. The thermal images were analyzed using Optris PIX Connect software (Rel.1.2.1030.0) with a thermal sensitivity (NETD) of 60 mK.

2.5. Icephobic properties

2.5.1. Photothermal de-icing under simulated sunlight

The photothermal de-icing performance of the coatings was evaluated using two distinct experimental setups under simulated solar irradiation: Gravity-driven ice sliding and droplet melting dynamics.

2.5.1.1. Gravity-driven ice sliding. In this approach, de-icing performance was evaluated using a fixed-angle inclined plane method to determine the time required for ice blocks to slide under photothermal heating. Planar ice blocks (39 × 39 mm) with varying thicknesses (3, 5, and 10 mm) were prepared using cubic molds by freezing water at −5 °C for 24 h. All experiments were conducted in a cold room maintained at −5 °C as illustrated in Fig. 2a. Upon exposure to the xenon light source, the ice removal time was recorded and defined as the interval between the onset of irradiation and the initiation of downward motion driven by the weight of the ice. Three trials were performed to analyze the impact of ice thickness.

2.5.1.2. Droplet melting dynamics. In this approach, a 100 μL droplet of distilled water was frozen on the coating at −10 °C to assess de-icing behavior at the microscale. Following freezing, the sample was irradiated with simulated sunlight. Upon irradiation, the solid-to-liquid phase transition was monitored via high-speed camera (MotionBLITZ, MIKROTRON, EoSens Cube 7, Germany) to extract the onset of de-icing (interfacial melting or mobility) and the total melting duration. Surface temperature was simultaneously tracked using an infrared (IR) camera as illustrated in Fig. 2b.

2.5.2. Ice adhesion strength and ice nucleation temperature

Ice adhesion strength was evaluated via a push-off test in a climate-controlled chamber at −10 °C. Cylindrical ice columns were formed by filling plastic molds (diameter: 10 mm) with deionized water and freezing them on the coating surface for 24 h. A digital force gauge (FG-3005, Shimpo Instruments, USA) connected to a computer interface was used to measure the shear force. The gauge probe applied force to the ice cylinder at a constant speed of 0.01 mm/s until detachment occurred. The probe was positioned 1 mm above the interface to minimize torque. Ice adhesion stress was calculated by dividing the maximum load by the

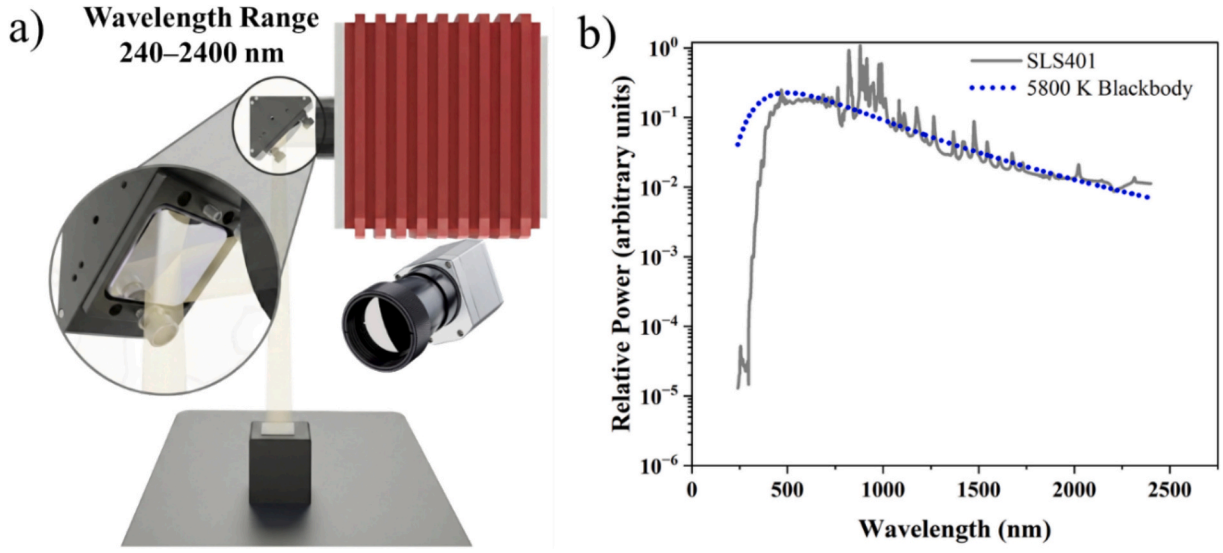


Fig. 1. (a) Schematic illustration of the solar simulator setup incorporating UV-Enhanced Aluminum Zerodur Mirrors. (b) Spectral power distribution of the SLS401 source compared to a 5800 K blackbody reference (The spectrum is presented on a logarithmic scale).

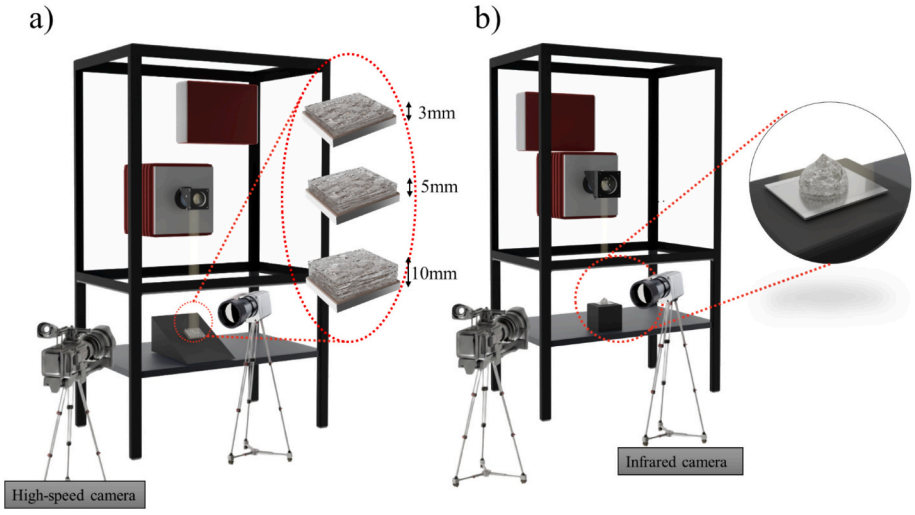


Fig. 2. Experimental setup of a) The fixed-angle inclined-plane method used to measure the sliding time of ice blocks with thicknesses of 3-, 5-, and 10-mm. b) The photothermal de-icing configuration for ice deroplets.

contact area. The icing/de-icing cycle was repeated 50 times on selected samples to assess mechanical durability. Ice nucleation temperatures were analyzed using Differential Scanning Calorimetry (DSC). A 5 mg water droplet was sealed in an aluminum pan coated with the sample and cooled from 30 °C to – 40 °C at 5 K/min.

2.5.3. Centrifugal ice adhesion testing

The push-off test measures the shear adhesion of ice formed by freezing stationary water, whereas the centrifugal adhesion test (CAT) evaluates spray-accreted ice under centrifugal loading. These methods therefore assess ice adhesion under different icing and loading conditions. The aluminum beams (6061-T6 alloy, 340 × 31.8 × 6.4 mm) were prepared, with three beams assigned to each coating. The coatings were applied at one end of each beam and cured at room temperature for seven days. Ice was deposited on the coated beams in a cold room at −8 °C for 30 min using a spray nozzle, with water supplied at 4 °C and an air pressure of 70 psi. The iced beams were then tested at −10 °C with a nominal rotational acceleration of 300 rpm s^{-1}. Ice adhesion strength was calculated as $\tau = m\omega^2 r/A$, where m is the detached ice mass, ω is the angular velocity at detachment, r is the effective radius, and A is the detached area [21]. Uncoated aluminum served as the reference.

2.5.4. Outdoor deicing under natural exposure

Outdoor deicing performance was evaluated in Chicoutimi, Quebec, Canada. The comparison included S17, a 10 wt% photothermal-only coating(S12) and neat PU (S2). Samples were mounted side by side on the same support at an inclination of 45°. Ice layers with a footprint of 39 × 39 mm and a thickness of 5.0 ± 0.2 mm were prepared in the laboratory and transferred outdoors. Before exposure, the specimens were conditioned in shade for 5 min. During exposure, air temperature was −7 ± 2 °C incident irradiance in the sample plane was 1043 ± 80 W m^{-2} and relative humidity was 65 ± 5%. Surface temperatures were recorded by infrared thermography. The start of exposure defined time zero. Ice-removal time was defined as the first sustained downward displacement of the ice block.

3. Results and discussion

3.1. Surface morphology and chemical composition

3.1.1. Wettability behavior

The interplay between surface chemistry and water molecules is fundamental to understanding the icephobic potential of hybrid coatings. The wettability characteristics reveal how the coatings interact with liquid water prior to freezing. Using the static water contact angle (WCA) and sliding angle (SA) data derived from the RSM-based DOE, Analysis of Variance (ANOVA) was conducted to identify the formulation parameters that significantly influence surface wettability. The ANOVA results confirmed that the selected regression models (2FI for WCA and Reduced Quadratic for SA) were appropriate, demonstrating high coefficients of determination ($R^2 = 0.94$ for WCA and $R^2 = 0.98$ for SA). Both models reliably predict the wettability response within the design space. To optimize the predictive capability of the models and ensure statistical accuracy, a backward elimination process was applied. The analysis initially included all main effects (copolymer content, nanoparticle content, and copolymer type) and their interactions. However, to refine the model and ensure statistical accuracy, terms with *p*-values greater than 0.05 (at a 5% significance level) were excluded from the analysis, as detailed in Table S1. Notably, the "Copolymer Type" (Factor C) also emerged as a statistically significant term (*p*-value = 0.0215), confirming that the specific molecular architecture (linear triblock of C25 versus graft-structured 626) distinctly influences the surface wetting regime.

In these statistical models, negative coefficients indicate an inverse relationship (increasing the parameter lowers the contact angle, enhancing hydrophilicity), while positive coefficients signify a direct relationship (increasing the contact angle). Based on the regression coefficients presented in Table S2 the statistical model indicates that the copolymer content (Factor A) exerts the most substantial influence on static wettability, exhibiting a strong negative coefficient of − 14.91. This negative correlation signifies that increasing the PEG/PDMS concentration significantly shifts the surface toward a hydrophilic state. This behavior is attributed to the hydration of PEG segments and their migration to the coating interface, where they interact with water molecules through hydrogen bonding [19]. Furthermore, the interaction term AB (Coefficient = − 13.29) reveals a synergistic effect between the copolymer and the nanoparticles. Comparing the two copolymer variants, the linear triblock structure of the C25 copolymer facilitated a more effective reduction in contact angle compared to the graft-structured 626. This is attributed to the linear C25 chains possessing higher mobility than the bulky graft structures of 626, allowing C25 to migrate more efficiently to the air-coating interface during the curing process. This negative correlation implies that higher concentrations of PEG/PDMS copolymer drive the surface toward a hydrophilic state, presumably due to the hydration of PEG segments. This pattern is clearly depicted in the 2D contour plots (Fig. 3a and d), where the blue regions of lowest contact angle (< 60°) correspond to formulations with high levels of both copolymer and nanoparticles. This behavior is attributed to the migration of the amphiphilic copolymer to the coating interface, where the hydrophilic PEG chains facilitate water spreading.

In contrast to the static WCA results, the nanoparticle content proved to be the dominant factor in reducing the Sliding Angle (SA), exhibiting a coefficient of − 4.20, compared to −2.78 for the copolymer content based on the data in Table S2. The contour plots for SA (Fig. 3b and e) show that the minimal sliding angles (< 10°) occur at the highest levels of nanoparticles and copolymers. This implies that although the surface becomes more hydrophilic, dynamic friction is minimized, likely through the formation of a lubricious Quasi-Liquid Layer (QLL) facilitated by the PEG/PDMS and the topological effects of the nanoparticles [22]. The linear configuration of C25 promotes the formation of a more uniform and stable hydration layer, which is essential for minimizing contact line pinning, whereas the steric hindrance of the graft-structured

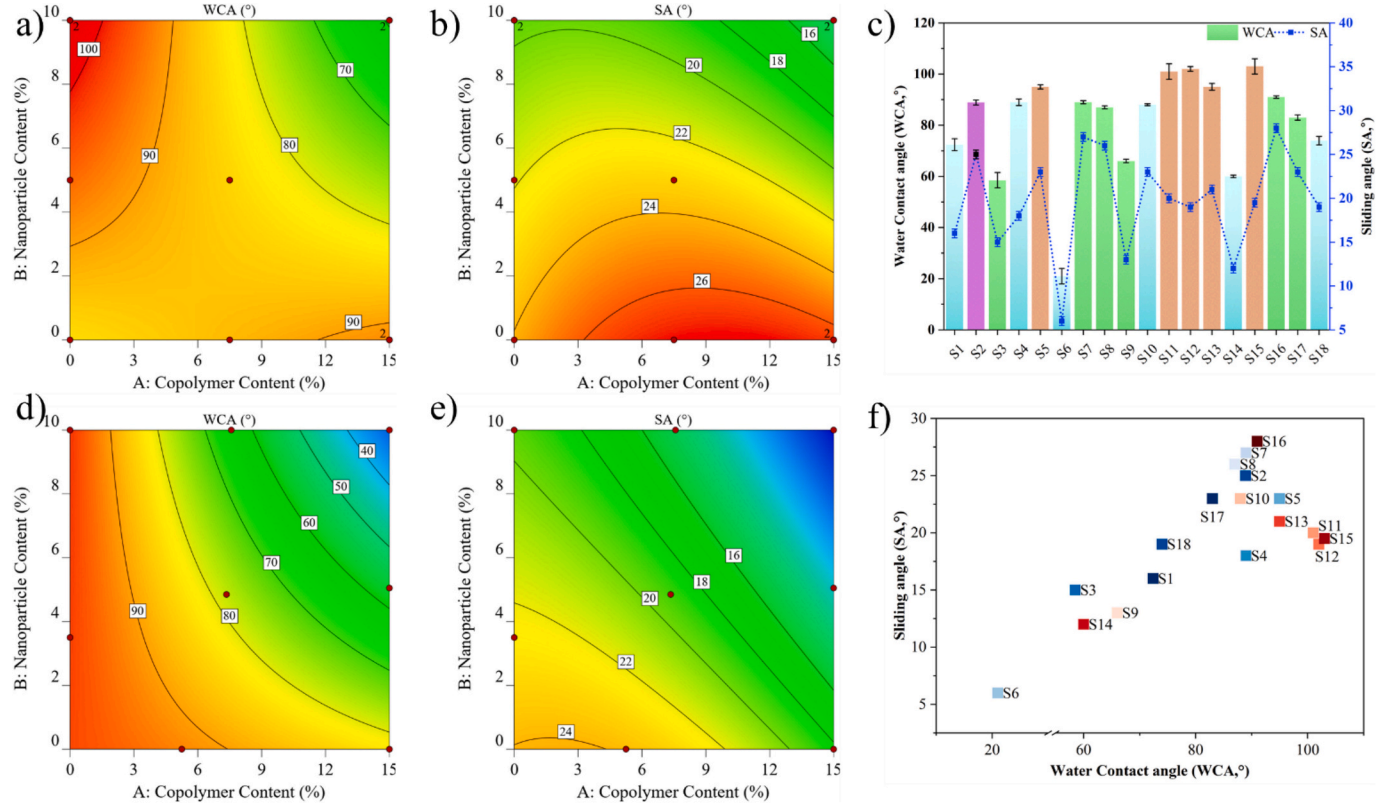


Fig. 3. (a, b, d, e) 2D contour plots illustrating the combined effect of nanoparticle and copolymer content on WCA and SA for the C25 (a, b) and 626 (d, e) series. (c) WCA and SA across all experimental formulations (S1–S18). (f) Scatter plot of SA versus WCA for all prepared samples (S1–S18).

626 appears to slightly impede this lubrication effect. Fig. 3c provides a comprehensive overview of the wetting characteristics for all 18 experimental formulations (S1–S18), displaying the variation in WCA alongside SA. Notably, formulation S6 exhibits a distinct "slippery hydrophilic" behavior, characterized by the lowest water contact angle in the series (< 25°) coupled with a minimal sliding angle (< 10°). In contrast, samples such as S11 and S15 show higher hydrophobicity but elevated sliding angles (> 20°), indicating a state where water droplets are more prone to pinning on the surface.

3.1.2. Surface roughness

The surface roughness (S_q) of the hybrid coatings was analyzed using a reduced quadratic model, which demonstrated a great fit to the experimental data with a coefficient of determination ($R^2 = 0.94$). To optimize the model's predictive capability, statistically insignificant terms were removed (stepwise elimination), resulting in a refined equation that excludes the quadratic effect of nanoparticle content (B^2) and the interactions between copolymer type and concentration (AC, BC), as shown in the ANOVA results (Table S1). The specific influence of each factor is quantified by the coded coefficients (Fig. 4c). Nanoparticle content (Factor B) exhibited the most substantial positive effect (+ 32.53), indicating that increasing the nanoparticle loading significantly amplifies surface roughness. This increase is attributed to the introduction of rigid nanostructures and potential micro-agglomerates that protrude from the coating surface [23,24]. Conversely, increasing the copolymer content (Factor A) demonstrated a significant smoothing effect (coefficient − 23.46). This is mechanistically consistent with the self-lubricating action of the PEG/PDMS chains: they surface-segregate to form a continuous, low-modulus film that drapes over the rigid Fe_3O_4 agglomerates, partially masking their topography [25]. Notably, the "Copolymer Type" (Factor C) was found to be statistically non-significant ("ns"), with a high *p*-value of 0.7221 and a negligible coefficient of + 1.12. This crucial finding implies that the surface roughness is independent of the specific molecular architecture (linear C25 vs. graft 626); both copolymers induce similar topological changes, and the variation in roughness is strictly dependent on the quantity of the amphiphilic copolymer rather than their specific chemical configuration. The striking similarity between the topological patterns in Fig. 4a and Fig. 4b visually corroborates the ANOVA finding that copolymer architecture (graft vs. linear) has no statistically distinguishable impact

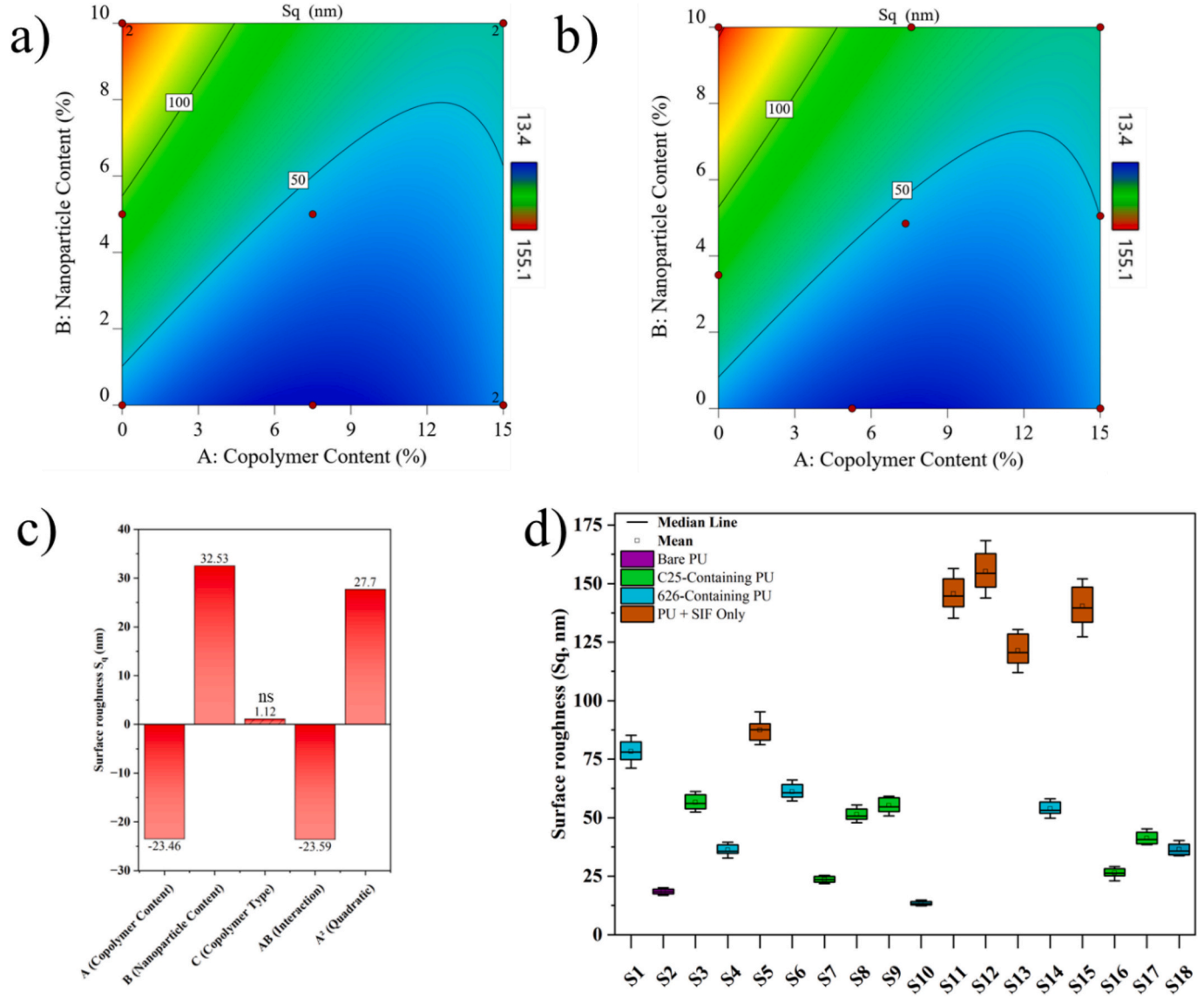


Fig. 4. The analysis of surface roughness (Sq) for the coating samples. (a, b) Contour plots showing how the roughness changes with different amounts of nanoparticles and copolymer for (a) C25 and (b) 626. (c) A chart showing the effect of each variable (A, B, C) and interaction terms (AB, A^2)on the roughness. (d) A box plot showing the range of roughness values for all samples (S1–S18).

on the resulting surface texture. The variations in surface topology across the 18 experimental formulations (S1–S18) are summarized in Fig. 4d. The box plot reveals distinct clustering where formulations devoid of copolymers, such as S11 (10% nanoparticles, 0% copolymer), exhibit roughness values exceeding 150 *nm*. This is physically manifested in Fig. 5 as sharp, jagged peaks for S11 and S12 and S15, indicative of nanoparticle effect in the absence of copolymer. In contrast, the introduction of PEG/PDMS copolymers drastically flattens the surface profile; formulations like S14 and S16 cluster at the bottom of the box plot (< 50 *nm*), appearing in Fig. 5 as smooth, uniform landscapes where the underlying nanoparticles are effectively buried [26,27].

3.2. Mechanical properties

Statistical analysis confirmed that the developed models describing the mechanical properties were significant, with coefficients of determination (R^2) of 0.89 for Young's modulus (Tables S7 and S10), 0.86 for tensile strength, and 0.87 for elongation at break (Tables S8–S10). The formulation parameters exhibited varying degrees of influence on these properties. To ensure robust statistical accuracy for the mechanical properties, the initial models were refined by systematically excluding statistically insignificant terms ($p > 0.05$ in Table S1). As detailed in Tables S7, S8, and S9, this backward elimination process focused on maximizing model fit by removing non-contributing factors. However, certain non-significant terms were retained solely to maintain hierarchical integrity where their corresponding interaction or quadratic effects were significant (e.g., retaining Factor A in Table S8 to support the significant A^2 term).

As illustrated in Fig. 6, the incorporation of the self-lubricating copolymer (Factor A) exerted the most dominant influence on the coating's stiffness. Specifically, increasing the copolymer content resulted in a substantial reduction in Young's Modulus (Coefficient: -23.41) and a variation in elongation at break. This softening effect is attributed to the introduction of flexible polysiloxane and polyether chains within the polyurethane matrix, which increases free volume and chain mobility [23]. While a lower modulus is often advantageous for minimizing ice adhesion strength via interfacial cavitation, it must be balanced against potential compromises in wear resistance [27]. Contrary to the reinforcement often observed in nanocomposites, the addition of silicone oil coated Fe_3O_4 (Factor B) in this system led to a decrease in both Young's modulus and tensile strength, as shown by the negative coefficients in the ANOVA (Fig. 6a and b). This trend suggests that at higher concentrations, the nanoparticles may have acted as stress concentration points rather than reinforcing agents, likely due to discontinuities in the polymer matrix or slight agglomeration [26,28]. However, a significant interaction effect (AB) was observed, particularly for Young's Modulus and elongation at break. As depicted in the 2D contour maps (Fig. 7), the simultaneous presence of copolymer and nanoparticles created a complex behavior where the negative impact of individual components was mitigated. For instance, Fig. 7c and f reveal that while nanoparticles alone reduced elongation, their interaction with the copolymer (positive AB term in ANOVA) helped retain coating flexibility. This suggests a unique interfacial interaction where the copolymer chains may encapsulate the nanoparticles, preventing severe embrittlement [26]. The chemical structure of the copolymer (Factor C: Type 626 vs. C25) played a subtle but statistically significant role, particularly in tensile strength.

As shown in Fig. 6b, formulations containing Type 626 (Factor C at +1 categorical level) generally exhibited superior tensile properties compared to Type C25. Additionally, the significant negative quadratic

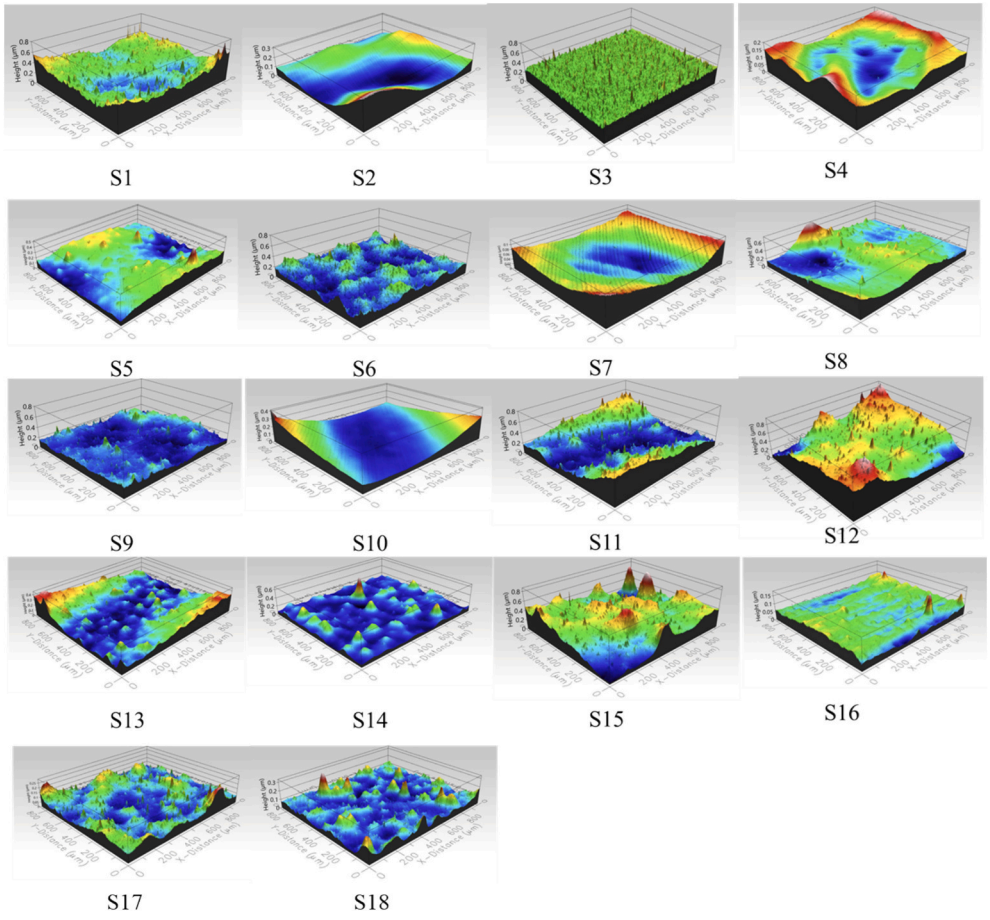


Fig. 5. 3D surface topography images of the prepared polyurethane hybrid coatings (Samples S1–S18).

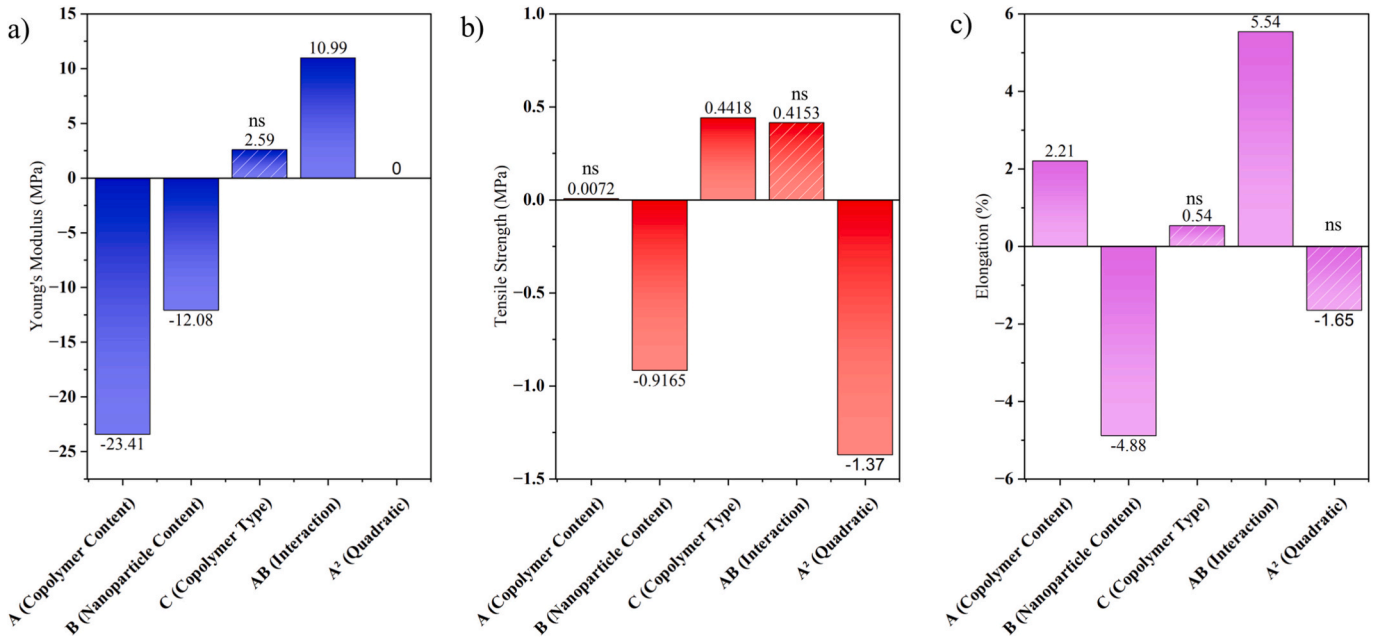


Fig. 6. Effect of formulation parameters on mechanical properties: (a) Young's Modulus, (b) Tensile Strength, and (c) Elongation at Break. Hatched columns represent non-significant effects.

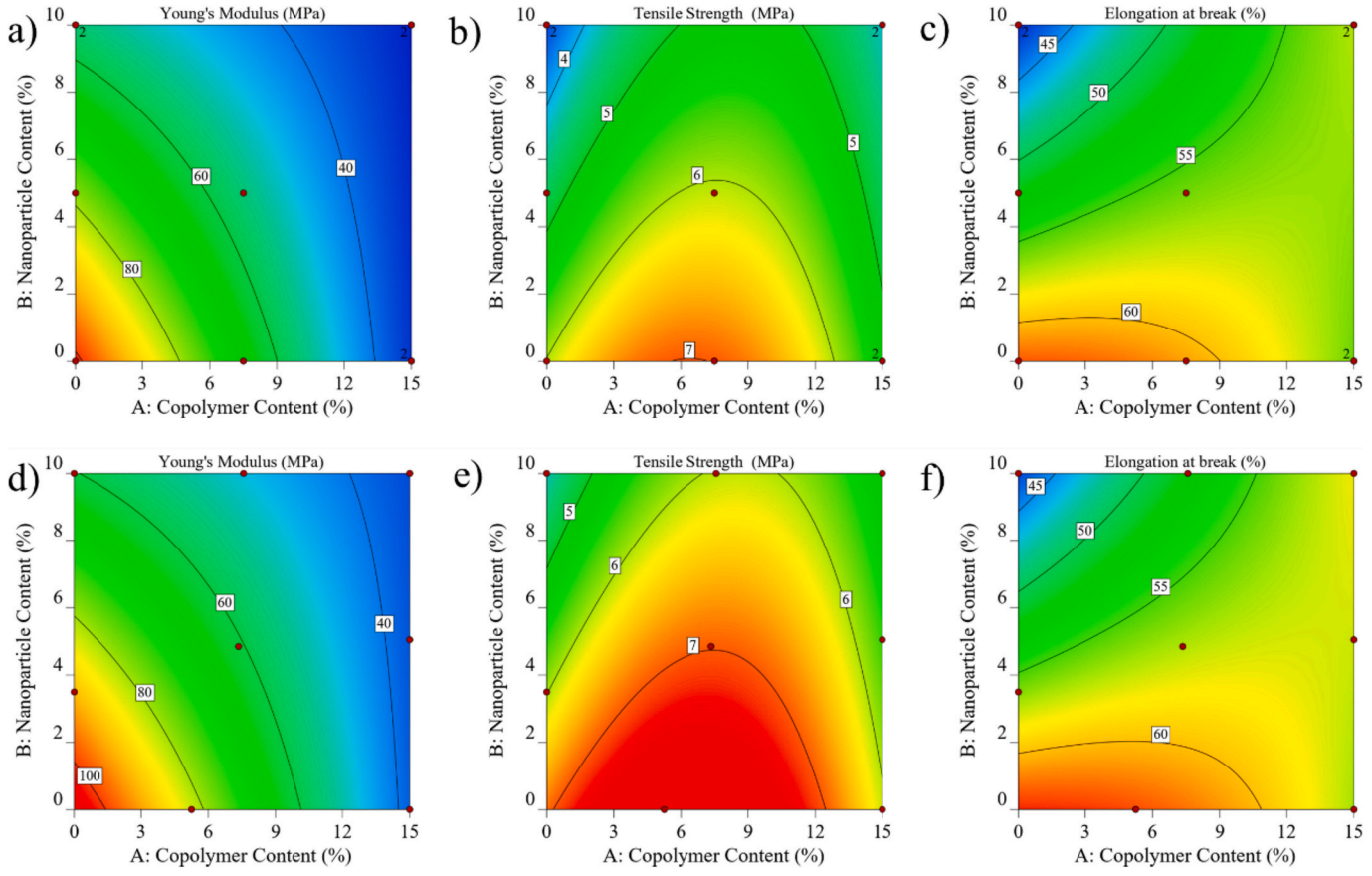


Fig. 7. 2D contour maps depicting the influence of formulation parameters on mechanical performance for copolymer C25 (a–c) and copolymer C626 (d–f). The plots display the trends for (a, d) Young's Modulus, (b, e) Tensile Strength, and (c, f) Elongation at Break, respectively. Colors represent the magnitude of the response (red = high, blue = low). (For interpretation of the references to colour in this figure legend, the reader is referred to the web version of this article.)

term for copolymer content (A^2 : − 1.37) in Fig. 6b implies a parabolic response with an optimum as shown in Fig. 7b-e. Below this optimum, the copolymer increases chain mobility and toughens the film; above it, the soft PEG/PDMS phase exceeds the percolation threshold of the rigid

PU hard segments, disrupting the load-bearing network and reducing tensile strength.This indicates that the 626 formulation possesses a more robust cross-linked network capable of better absorbing deformation energy under stress [25]. The DoE analysis identifies a trade-off. The most mechanically stable coatings were those that leveraged the AB interaction to balance stiffness and flexibility. The contour plots in Fig. 7 suggest that an intermediate region (optimizing the ratio of copolymer to nanoparticles) offers the most favorable configuration. This balance minimizes the modulus sufficiently for ice removal while retaining enough structural integrity to withstand icing/de-icing cycle [29].

3.3. Photothermal properties

Response Surface Methodology (RSM) was used to analyze the surface temperature rise after 20 min (ΔT_{20}) under simulated solar irradiation to determine the factors influencing the solar-to-thermal conversion efficiency of the coatings. By 20 min, the surface has reached a quasi-steady state in which absorbed solar power equals the radiative + convective heat-loss rate from the coupon; ΔT_{20} therefore serves as a proxy for the steady-state solar-to-thermal conversion capacity of the coating under realistic outdoor solar flux. At first, the experimental data were put into a full quadratic model that included all possible main effects, quadratic terms, and two-way interactions. However, looking at the first ANOVA showed that some terms, like copolymer content (Factor A), copolymer type (Factor C), and relationship terms (AC, BC), were not statistically significant ($p > 0.05$). As illustrated in the 2D contour plot and 3D response surface in Fig. 8a and b, the temperature rise is almost exclusively dependent on the nanoparticle concentration (Factor B). In the results, it is observed that the addition of the PEG/PDMS copolymer (Factor A) has a negligible or non-detrimentaleffect on the steady-state equilibrium temperature. Formulations with high copolymer content (15%), such as S3 and S9, reached thermal equilibrium levels nearly identical to those of copolymer-free samples with the same nanoparticle loading, such as S12 and S15.

To adhere to the principle of parsimony and improve the model's predictive accuracy, these non-significant factors were removed via backward elimination. The final analysis was conducted using a reduced quadratic model, which retained only the significant terms and those required to support hierarchy. The refined model demonstrated an exceptional fit to the experimental data, yielding a high coefficient of determination ($R^2 = 0.97$). Analysis of Variance (ANOVA) and Regression Coefficients The ANOVA results (Table S15) unequivocally identify the Nanoparticle Content (Factor B) as the dominant factor influencing the surface temperature. The quadratic term for nanoparticles (B^2) showed a slight negative coefficient (− 2.1), indicating a minor plateauing effect at higher concentrations. This phenomenon is likely due to the "inner filter effect" or optical saturation, where nanoparticles in the upper surface layers absorb most incident light, shielding those deeper in the matrix and marginally reducing the heating efficiency per unit mass at high loadings [30]. The initial heating rate (dT/dt), determined from the slope of the temperature rise during the first 30 s of irradiation, was calculated as 8.61 °C/min for sample 17 and 7.20 °C/min for sample 5 (Fig. 9). Higher nanoparticle loading accelerates initial heating. Overlapping curves from samples with and without copolymer prove it never hinders photothermal performance.

3.4. Anti-icing properties

3.4.1. Ice adhesion

Fig. 10a illustrates the relative impact of each formulation variable on ice adhesion strength, while the experimental results for ice adhesion strength across all design runs are summarized in Fig. 10b. These results were obtained using the push-off test. The experimental results, analyzed using a reduced quadratic model ($R^2 = 0.96$), reveal that the formulation parameters significantly dictate the anti-icing properties (As detailed in the Table S11, S12). As explicitly shown in the coefficient bar chart (Fig. 10a), the copolymer content (Factor A) exhibited a strong negative coefficient (− 69.16), indicating that increasing the concentration of the PEG/PDMS copolymer was associated with lower ice adhesion strength. This relationship is visually supported by the response surface plots in Fig. 11, where the surface drops steeply into the low-adhesion "blue zone" as copolymer content rises. This trend is consistent with two possible contributions: the formation of a quasi-liquid layer by the hydrophilic PEG segments, which acts as a lubricant at the ice-coating interface, and the reduction of the coating's elastic modulus (as seen in Fig. 6a), which facilitates ice removal via interfacial cavitation [23,27]. Coatings with high copolymer content, such as S3 and S9, consistently displayed lower ice adhesion strength-values compared to the bare PU (S2).

Conversely, the addition of photothermal nanoparticles (Factor B) showed a complex influence on ice adhesion. While the photothermal effect is beneficial for active de-icing, the rigid nature of the nanoparticles can increase the coating's stiffness and surface roughness (as confirmed by the roughness analysis). Higher roughness can lead to mechanical interlocking with ice, potentially increasing adhesion strength if not properly mitigated by the lubricating copolymer [31].

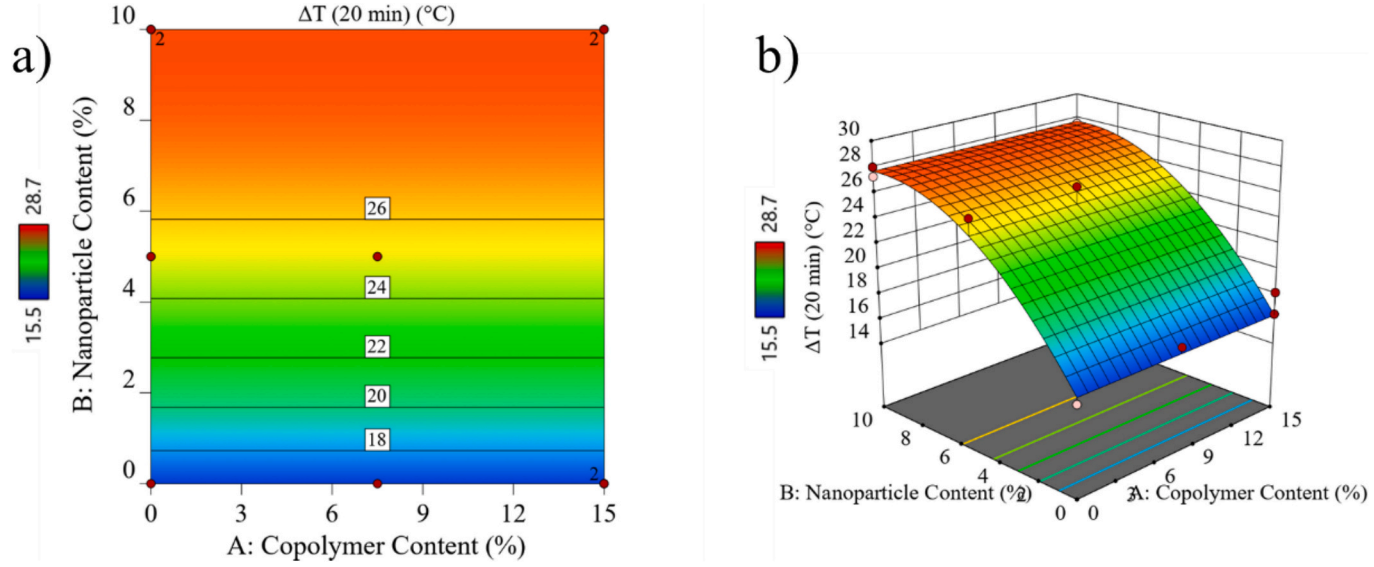


Fig. 8. (a) 2D contour plot and (b) 3D response surface plot showing the surface temperature rise (ΔT_{20min}) after 20 min of exposure.

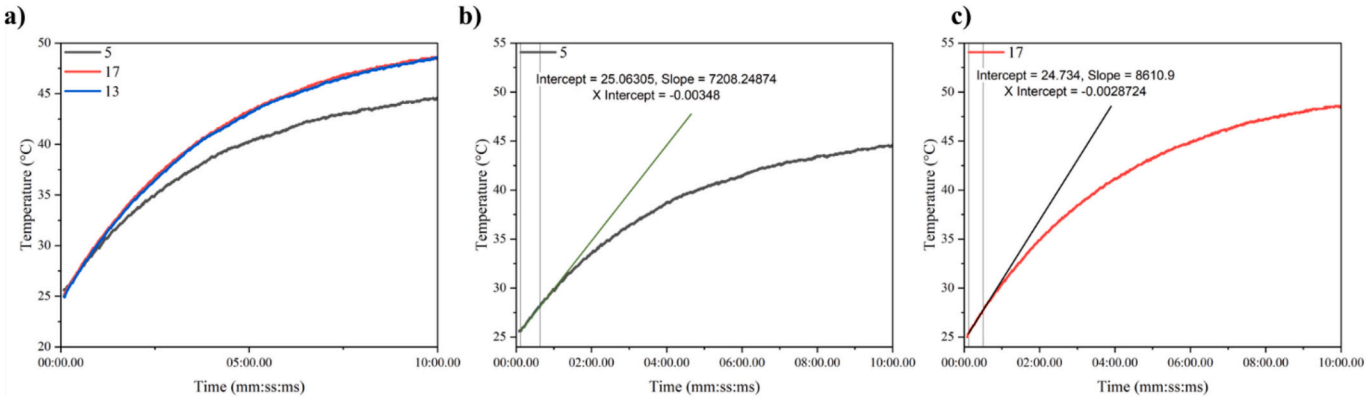


Fig. 9. (a) Temperature evolution over time for samples S 5, S17, and S13. Sample 5: 0% copolymer, 3.5% SiF; Sample S17: 7.5% copolymer, 5% SiF; Sample S13: 0% copolymer, 5% SiF. (b) Sample S5 with slope line fitted to the initial 30 s interval. (c) Sample S17 with slope line fitted to the initial 30 s interval.

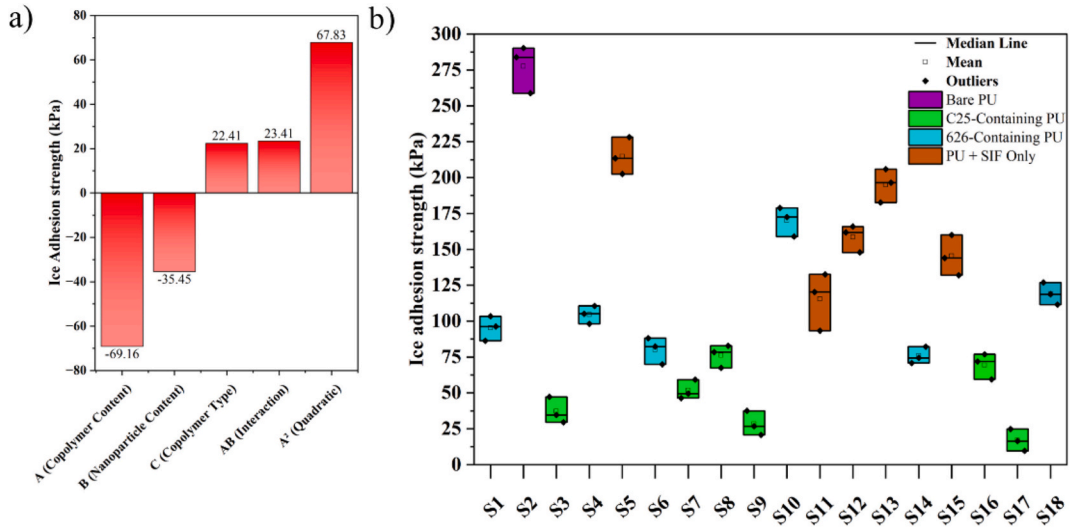


Fig. 10. (a) A bar chart showing the effect of different variables on the adhesion strength (b) Box plots of all experimental for all samples (S1–S18).

However, the significant interaction term (AB) in the ANOVA model demonstrates that the copolymer successfully counteracts this negative effect. It is likely that the soft copolymer phase effectively encapsulates the nanoparticles, masking their physical roughness and preventing them from acting as anchoring points for ice [26]. This interaction is critical for achieving low ice adhesion of hybrid coatings. Active mechanism is absent in copolymer-only formulations such as S4 and S16, rendering them reliant solely on passive lubrication, which may be insufficient under extreme icing conditions where interfacial freezing occurs.

The distinct behavior of the copolymer types (Factor C) further refined the icephobic performance. The linear triblock copolymer (C25) generally outperformed the graft copolymer (626) in reducing ice adhesion, likely due to the higher mobility of its linear chains, which may reflect differences in chain mobility and surface segregation that favor interfacial lubrication [19]. This aligns with the wettability findings, where C25 formulations generally exhibited lower contact angles and sliding angles.

Crucially, sample S17 (7.5% Copolymer, 5% Nanoparticles, Type C25) emerged as a top-performing formulation, exhibiting an optimal balance of properties. With an ice adhesion strength of approximately (17 ± 7) kPa, S17 rivals the performance of the lowest ice adhesion samples like S14 and S16 but offers superior mechanical durability. While S16 (15% Copolymer, 0% Nanoparticles) achieved low ice adhesion due to its very low modulus and high lubrication, its lack of reinforcing nanoparticles resulted in poor wear resistance and tensile strength and lacks the photothermal capability. In contrast, S17 leverages the synergistic AB interaction, while the 5% nanoparticle loading imparts necessary mechanical reinforcement (higher Young's Modulus and Tensile Strength than S16) without causing significant embrittlement or roughness-induced interlocking.

Complementary CAT measurements also showed lower ice adhesion for the hybrid coatings than for the reference surfaces. Averaging the repeated CAT results obtained on the same beams gave ice adhesion strengths of 78.6 ± 17.5 kPa for S17 and 84.2 ± 10.7 kPa for S3, compared with 507.7 ± 18.9 kPa for uncoated aluminum and 543 ± 20.4 kPa for neat PU. These values correspond to approximately 85.5% and 84.5% lower adhesion than neat PU for S17 and S3, respectively. Although the absolute CAT values were higher than those obtained by push-off testing, both methods showed reduced ice adhesion for the hybrid formulations relative to neat PU. The difference in magnitude reflects the different testing conditions: CAT evaluates spray-accreted ice under centrifugal loading, whereas the push-off test measures the detachment of ice formed by freezing stationary water. The CAT results therefore extend the observed benefit of the hybrid formulations to a second icing and loading configuration.

3.4.2. Durability: icing / de-icing cycles

To evaluate the long-term operational stability of the formulated coatings, a 50-cycle icing/de-icing durability analysis was conducted at

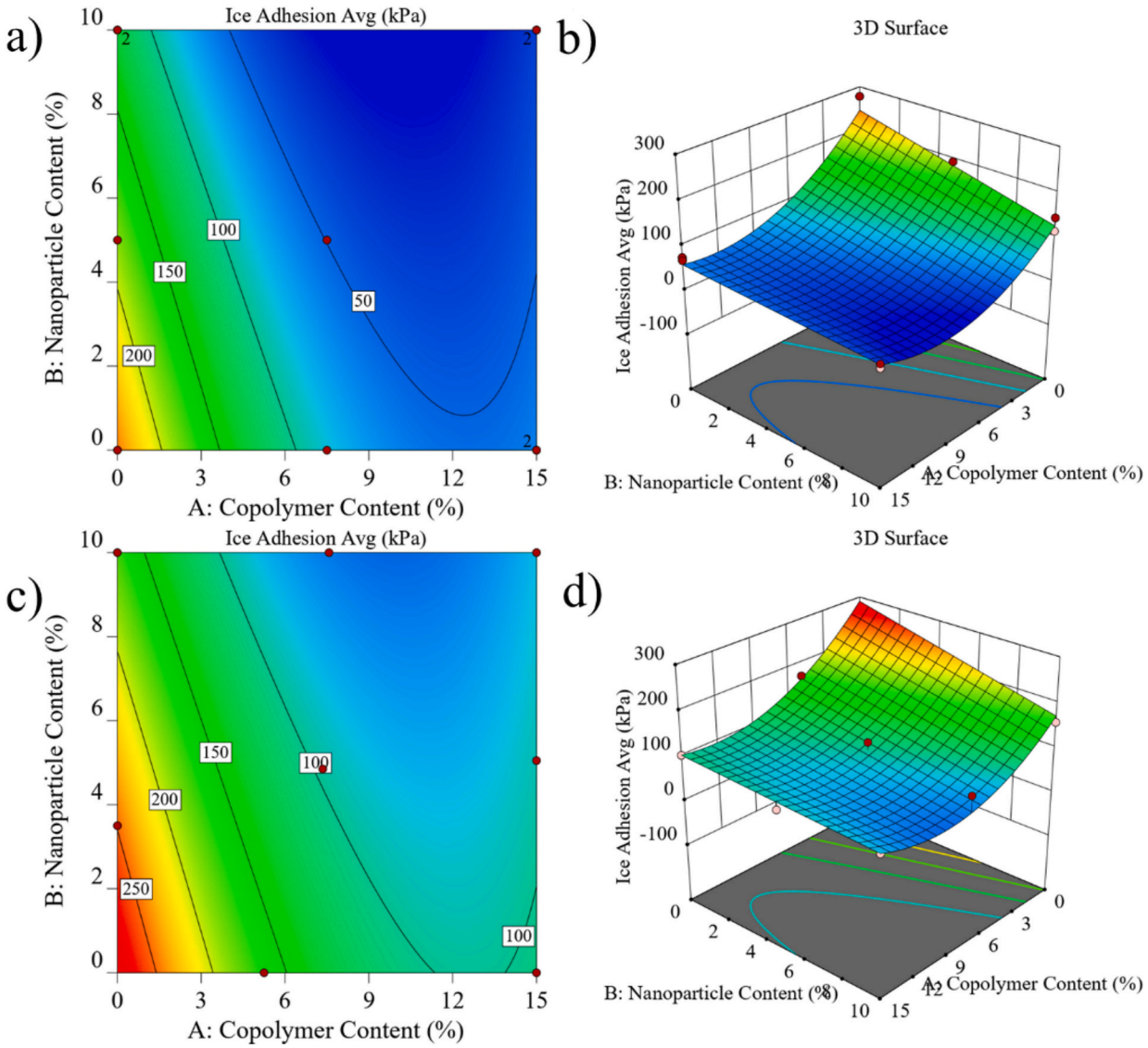


Fig. 11. Analysis of ice adhesion strength. (a, b) 2D and 3D plots for Copolymer C25. (c, d) 2D and 3D plots for Copolymer 626.

−10 °C, with IAS Growth Rate summarized in Table 3. The unmodified polyurethane reference, S2, established a baseline per-cycle degradation slope of 1.84 kPa cycle^{-1} and a fifty-cycle mean ice adhesion strength of 317 kPa. The active-only sample with a high nanoparticle loading (S12, 10% SIF) deteriorates rapidly at a rate of 5.42 kPa cycle^{-1}, crossing the bare PU performance envelope by cycle 35 and reaching a final value of 429 ± 20 kPa. This indicates that mechanical interlocking becomes stronger with repeated icing-deicing cycles, making it less appropriate for long-term anti-icing applications. The passive-only formulation (S16, 15% C25), by contrast, exhibits a markedly shallower degradation slope of 0.90 kPa cycle^{-1}, owing to the sustained quasi-liquid layer generated by the amphiphilic PEG/PDMS chains, though it nonetheless approaches the 100 kPa icephobic threshold in the vicinity of cycle 25.

Table 3
Per-cycle degradation metrics over 50 icing / de-icing cycles at −10 °C.

Sample	Initial IAS (kPa)	IAS at Cycle 50 (kPa)	IAS Growth Rate (kPa/cycle)	50-cycle mean (kPa)
S17	17 ± 7	28 ± 10	0.22	21
S3	37 ± 9	63 ± 12	0.52	50
S6	80 ± 9	125 ± 14	0.91	102
S16	70 ± 9	115 ± 14	0.90	92
S13	195 ± 11	345 ± 18	2.99	270
S2	271 ± 9	363 ± 15	1.84	317
S12	158 ± 10	429 ± 20	5.42	293

The synergistic advantages of combining active photothermal method with passive self-lubrication are clearly demonstrated by the hybrid formulations, which consistently operate within the high-performance, low-adhesion regime illustrated in the lower portion of Fig. 12. A direct comparison of the graft copolymer hybrid S6 (15% 626 + 10% SIF) and its linear counterpart S3 (15% C25 + 10% SIF) reveals a significant architectural effect: the linear diblock ester backbone confers superior amphiphilic chain mobility, resulting in a more rapidly replenishing quasi-liquid layer during the de-icing phase and a per-cycle degradation slope that is roughly half that of the graft structure. The response surface methodology-optimized hybrid S17 (7.5% C25 + 5% SIF) defines the optimal anti-icing durability profile. Commencing at an ultra-low ice adhesion strength of 17 ± 7 kPa, this formulation degrades at a negligible rate of 0.22 kPa cycle^{-1} and sustains a 50-cycle mean of 21 kPa (15-fold lower than the bare polyurethane baseline). It is below the conventional 100 kPa threshold throughout the entire test duration. The lower rate of increase in ice adhesion for S17, compared with the nanoparticle-only and copolymer-only formulations, demonstrates improved resistance to the loss of

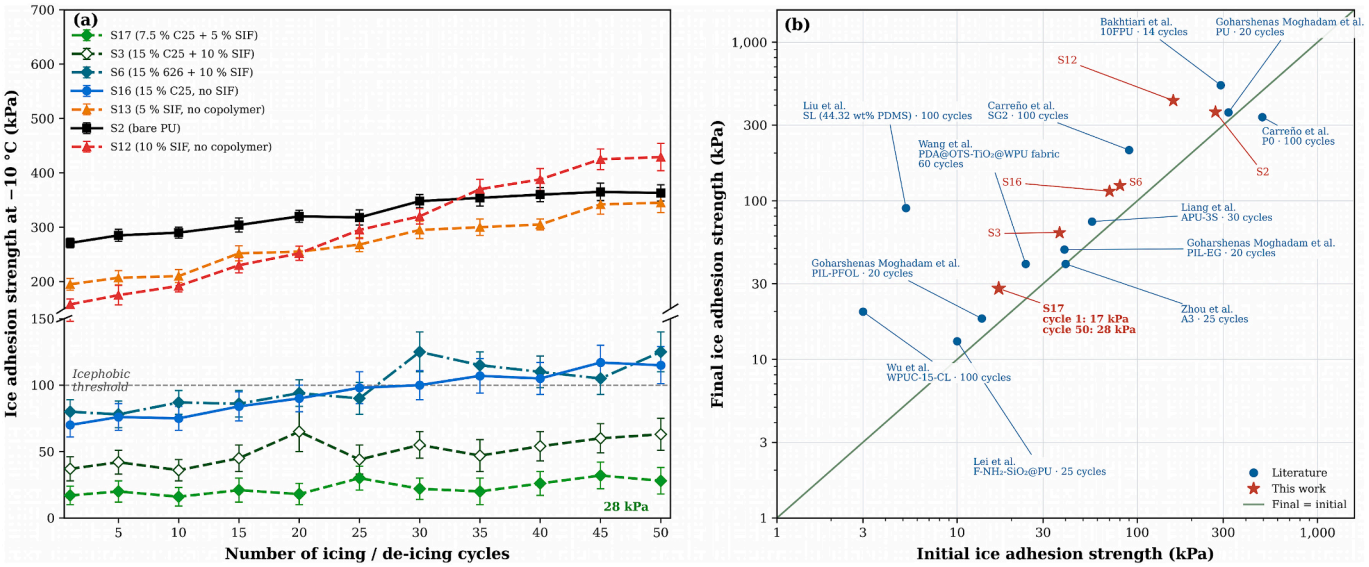


Fig. 12. a) Ice adhesion strength (IAS) ofselected Samples over 50 ice/de-icing cycles, obtained by push-off tests. b) Initial versus final ice adhesion strength for the present coatings after 50 icing/de-icing cycles (red stars) and literature coatings after the indicated cycle numbers (blue circles). The dashed line denotes unchanged adhesion. (For interpretation of the references to colour in this figure legend, the reader is referred to the web version of this article.)

icephobic performance during repeated icing and mechanical ice removal. Together with the mechanical results, this behavior identifies the optimized hybrid as a formulation that combines low ice adhesion with mechanical integrity and sustained ice-release performance.

The literature comparison in Fig. 12b places the retained ice adhesion of S17 within the range achieved by other polyurethane-based icephobic coatings [20,32–40]. Liang et al. [36] reported an initial adhesion of approximately 56 kPa for their PDMS-modified acrylic polyurethane coating, APU-3S, reaching a maximum of 74 kPa during 30 icing/de-icing cycles. The 28 kPa endpoint of S17 after 50 cycles therefore compares favourably in absolute adhesion, although the tests were conducted under different protocols. Lower adhesion has also been reported: Wu et al. [39] demonstrated adhesion below 20 kPa in 85% of the measurements across 100 cycles for a *comb*-like waterborne polyurethane. These benchmarks highlight the need to consider retained adhesion alongside cycling duration. S17 combines a low final adhesion with endurance over 50 cycles, while differences in temperature, ice geometry, loading conditions, and cycling procedures limit direct durability rankings across studies.

3.4.3. *Ice formation temperature*

The ice formation temperature T_{IF}, as determined by Differential Scanning Calorimetry (DSC), served as the primary response variable. This parameter is critical for anti-icing applications, as a lower T_{IF} indicates an enhanced ability to delay the liquid-to-solid phase transition of water under supercooled conditions [21]. The statistical significance of the developed model and individual factors was assessed via ANOVA, as summarized in Table S13. As shown in Table S10, the fit statistics demonstrate a correlation between the experimental and predicted data. The Coefficient of Determination (R^2) was calculated as 0.98. According to the ANOVA results, Copolymer Content (A) and Nanoparticle Content (B) were identified as the most significant terms ($p < 0.0001$), highlighting their dominant role in determining the freezing delay. The influence of these variables is visually represented in the contour plots in Fig. 13(a, b) and quantified by the regression coefficients in Fig. 13c. The regression equation provided in Table S14

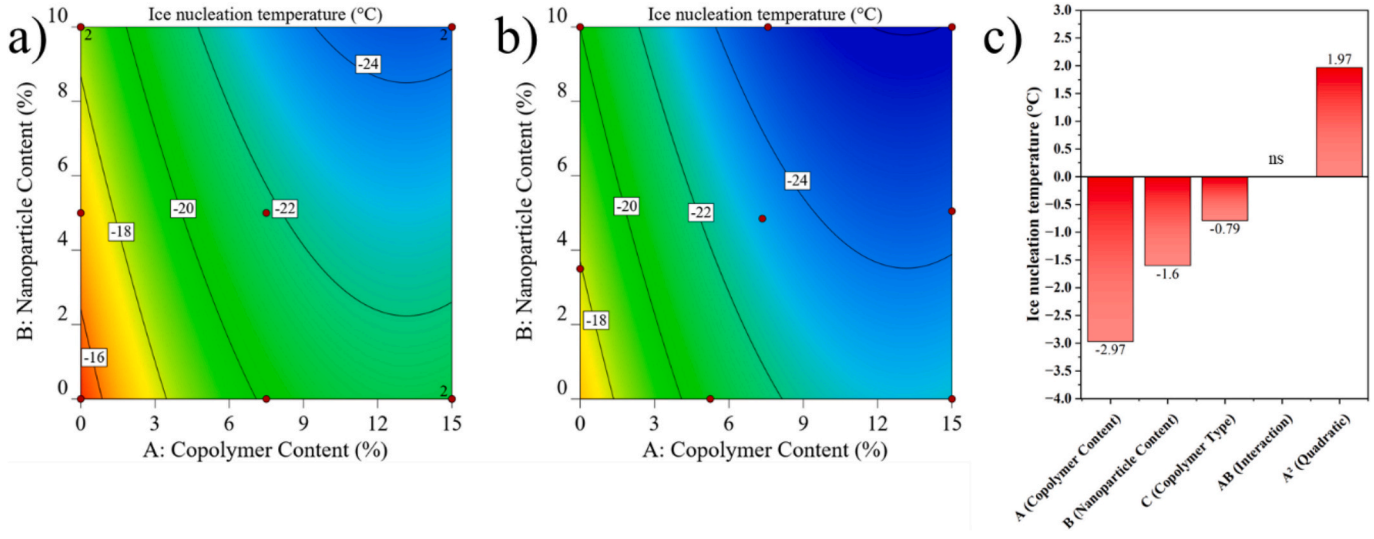


Fig. 13. (a, b) Contour plots showing the freezing temperatures for samples containing (a) C25 and (b) 626. (c) A chart showing the effect of each variable on ice nucleation temperature.

($T_{IF} = -22.56 - 2.97A - 1.60B - 0.7954C + 1.97A^2$) reveals that both copolymer content and nanoparticle content have negative coefficients, meaning that increasing their levels leads to a decrease in the ice nucleation temperature. As shown in the box plot in Fig. 14a, there is a distinct variation in freezing temperatures across the samples (S1–S18), with modified surfaces generally exhibiting lower nucleation temperatures compared to the bare PU. The DSC thermograms presented in Fig. 14b further illustrates this delay. As a baseline, the control sample S2 (Pure Polyurethane), exhibited −14.67 °C ice formation temperature due to hydrogen bonding between water molecules and the polar urethane groups, which creates a "quasi-liquid layer" (QLL) that delays nucleation [41]. The introduction of A and B significantly depressed T_{IF}, albeit through distinct mechanisms. The S15 (0% Copolymer, 10% Nanoparticles) demonstrated a notable reduction in freezing temperature compared to the control. This effect is attributed to the silicone oil coating on the Fe_3O_4 nanoparticles [42]. by interacting with water droplets and reducing the number of ice nucleation sites . Conversely, the S16 (15% Copolymer, 0% Nanoparticles) achieved a similar or greater depression in T_{IF}through a chemical inhibition mechanism. The amphiphilic PEG/PDMS copolymer migrates to the surface, where the hydrophilic PEG segments bind interfacial water molecules to form a quasi-liquid layer (QLL). This hydration shell acts as a thermodynamic buffer, disrupting the tetrahedral ordering of water and energetically favoring the liquid phase even at sub-zero temperatures [21,43].

In hybrid formulations, the combination of these mechanisms resulted in the superior performance observed in S3 (15% Copolymer, 10% Nanoparticles, Type C25), which exhibited one of the lowest nucleation temperatures. However, when comparing S3 with S1 (7.58% Copolymer, 10% Nanoparticles, Type 626), the influence of the copolymer architecture becomes evident. Interestingly, samples containing the Type 626 copolymer (such as S1 and S6) generally demonstrated a more pronounced ability to suppress ice nucleation compared to the linear C25 variants. This can be attributed to the graft molecular architecture of Type 626. Compared to the linear chains of C25, the branched graft architecture of Type 626 may introduce additional steric hindrance and conformational disorder at the interface, potentially imposing an entropic cost on the ice crystallization process and thereby hindering the formation of stable ice nucleus [44].

From a statistical perspective, the Design of Experiments (DOE) analysis revealed a crucial distinction in the behavior of T_{IF} compared to mechanical properties: the interaction term AB (*Copolymer* × *Nanoparticle*) was found to be statistically insignificant. This indicates that, for ice nucleation temperature, the additives operate via an additive model rather than a synergistic one. Physically, this suggests that the chemical disruption of the water lattice by the copolymer and the surface energy reduction by the nanoparticles occur independently. The copolymer functions at the molecular level to inhibit embryo growth, while the nanoparticles modify the macroscopic surface wettability [45,46]. Since nucleation is a localized phenomenon governed by the "weakest link" (the most active defect site), saturating the surface with either additive provides a reduction in T_{IF} but combining them does not exponentially multiply the effect, as the nucleation barrier can only be raised to the limit of homogeneous nucleation [47].

3.4.4. *Anti-icing properties under simulated sunlight*

The effect of ice thickness on the anti-icing and de-icing properties of the developed hybrid coatings was evaluated using the gravity-driven ice-sliding test (Fig. 2a). The interfacial shear stress imposed by the ice block's own weight follows Eq. (1):

$$\tau = (\rho g h)\sin\theta_c \quad (1)$$

where τ is the interfacial shear stress (Pa), $\rho = 917\ kg/m^3$ is the density of ice, gravitational acceleration $g = 9.81\ m/s^2$, h = ice thickness and a slope angle of 30° where $\sin\theta_c = 0.5$. The plate area cancels because τ is a stress (force per unit area); for completeness, the corresponding equivalent force $A = 39mm \times 39mm = 0.001521\ m^2$. Table 4 summarizes the calculated interfacial shear stresses and equivalent forces corresponding to different ice thicknesses, based on the Eq. (1). Increasing ice thickness from 3 mm to 10 mm raises the gravitational shear stress on the interface from 13.49 Pa to 44.98 Pa, and the gravitational driving force on the ice block from 0.020 N to 0.068 N. This force is not externally applied; it is

Table 4
Calculated interfacial shear stress τ and equivalent force for ice blocks of varying thicknesses on surfaces.

Thickness t (mm)	Shear stress τ (Pa)	Equivalent force $F = \tau \cdot A$ (N)
3	13.49	0.02052
5	22.49	0.03421
10	44.98	0.06841

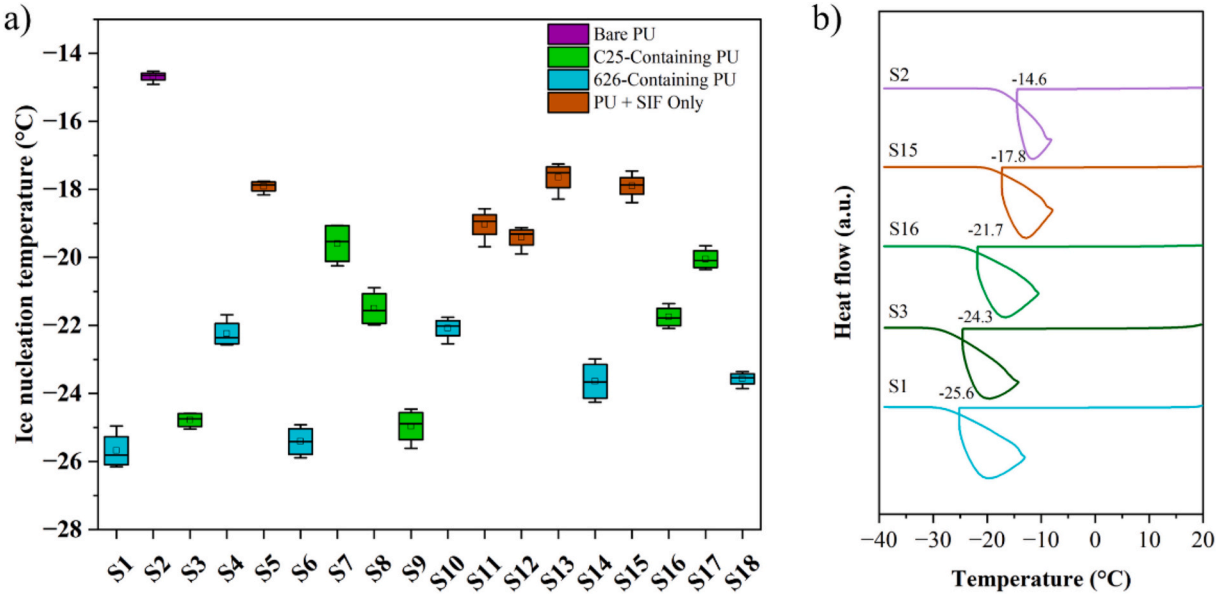


Fig. 14. The analysis of delayed ice nucleation temperature for the coating samples. (a) Box plot showing the freezing temperatures for all samples (S1–S18). (b) DSC thermograms for selected samples (S2, S15, S16, S3, S1), showing the specific freezing peaks and their onset temperatures.

the downslope component of the ice block's own weight. The implication is that thicker ice is easier to slide once the interfacial adhesion has been reduced sufficiently, but reaching that reduced adhesion requires the photothermal layer to melt the ice–coating interface fast enough that the residual adhesion drops below the new (higher) shear stress. This is why the de-icing time increases sub-linearly with ice thickness in Table 4.

The results (Table 5) demonstrate a correlation between ice thickness, and ice removal time. When ice with a thickness of 3 mm moved after 24 ± 2 min (Sample 6, containing copolymer 626), this indicates that simulated solar radiation reduced the ice adhesion strength to below the calculated shear stress of 13.49 Pa after 24 ± 2 min. At this point, the gravitational force exceeded the residual adhesion, enabling the ice to slide. For thicker ice layers of 5 mm and 10 mm, the corresponding removal times increased to 30 ± 5 min and 35 ± 3 min, respectively. This trend indicates that although gravitational driving force increases with ice thickness, longer irradiation is required to reduce adhesion to a critical threshold, as light penetration and interfacial melting become less efficient in thicker ice. This reduction in ice adhesion is attributed to the formation of a superficial water layer from melted ice at the ice–coating interface. Additionally, the presence of hydrophilic groups in the polyurethane coatings, such as urethane linkages and PEG/PDMS copolymer chains, enhances hydrogen bonding with water molecules, delaying freezing and promoting QLL formation. As noted in Section 3.4.1, the linear triblock structure of copolymer DBE-C25 allows more efficient migration of copolymers to the surface than the grafted structure of CMS-626, resulting in consistently shorter ice removal times for C25 compared to 626 [19]. According to the data presented in Table 5, a faster ice removal time was observed for coatings containing the C25 copolymer compared to the 626 coating across all thicknesses. Specifically, for 3 mm of ice, a removal time of 21 ± 2 min was recorded for Sample 3, which contained C25, whereas 24 ± 2 min was required for Sample S6, which contained the 626 copolymers.

The influence of surface chemistry is further highlighted by the poor performance of coatings lacking copolymers (Sample S13), where 3 mm ice required 145 ± 8 min for removal, and by Sample 16, where no removal was observed within 180 min. Furthermore, the synergistic effect of combining these two components is most remarkably demonstrated by Sample 17. Formulated with 7.5% C25 copolymer and 5% nanoparticles, Sample 17 exhibited the fastest ice removal time of just 12 ± 3 min for 3 mm ice. This exceptional performance, especially when compared to S3 and S6 with higher loadings, indicates that an optimized concentration balance is crucial. These results confirm that both photothermal effects and presence of copolymer are essential for efficient ice removal. In summary, two competing effects govern the de-icing process: (i) thinner ice exhibits lower gravitational force but allows more effective solar penetration and faster heat transfer to the interface, while (ii) thicker ice benefits from greater gravitational force but requires longer irradiation to sufficiently reduce adhesion due to reduced heat reach at the interface. Consequently, removal time increases moderately with ice thickness, despite the higher driving force from gravity. Importantly, the developed coatings maintained photothermal functionality for ice layers up to 10 mm, demonstrating practical applicability under moderate icing conditions.

Table 5
Ice removal times for coatings with different copolymer types and ice thicknesses (NR = No removal observed within 180 min of testing).

Sample	Copolymer Content (%)	Nanoparticle Content (%)	Copolymer Type	Ice Thickness (mm)	Ice Removal Time (min)
S2	0	0	–	3	NR
S6	15	10	626	3	24 ± 2
S6	15	10	626	5	30 ± 5
S6	15	10	626	10	35 ± 3
S3	15	10	C25	3	21 ± 2
S3	15	10	C25	5	25 ± 3
S3	15	10	C25	10	29 ± 4
S13	0	5	–	3	145 ± 8
S17	7.5	5	C25	3	12 ± 3
S16	15	0	C25	3	NR

3.4.5. Outdoor icingand deicing performance

Fig. 15 and Supplementary Video S1 compares the evolution of snow coverage on bare aluminum, S2, S3, S12, S17, and a commercial coating with PU during approximately 90 min of outdoor exposure at −10 °C and a light intensity of 135 ± 15 W/m^2. Bare aluminum, neat PU, and the commercial coating progressively developed extensive snow coverage, whereas S3, S13, and S17 retained larger exposed surface areas through much of the observation period. Snow accumulation became more pronounced on these three samples toward the end of the experiment, although portions of their surfaces remained visible. These observations suggest that S3, S12, and S17 limited snow coverage under the tested conditions; however, the images alone cannot establish whether this behavior resulted from photothermal heating, reduced snow adhesion, or a combination of mechanisms.

Fig. 16 and Supplementary Video S2 demonstrate the retained outdoor de-icing performance of the coatings after 50 ice push-off cycles. Under a cloudless sky, at a solar irradiance of 1043 ± 80 W/m^2 and a forecast ambient air temperature of approximately −10 °C, ice released from S17 after 213 s and from S12 after 233 s, giving S17 a 20 s shorter release time. Despite releasing ice later, S12 reached a higher camera-indicated temperature at 671 s (21.1 °C) than S17 (17.1 °C), consistent with its higher loading of photothermal nanoparticles; the commercial white PU coating reached 4.7 °C. The earlier ice release from S17 indicates that the final surface temperature alone does not determine de-icing time and suggests that interfacial ice-release behavior also contributes to performance. Successful ice shedding after repeated push-off testing supports the durability of S12 and S17 under the real outdoor conditions examined. The complementary time-lapse recording of snow accumulation is provided in Supplementary Video S1.

Together, the outdoor experiments demonstrate distinct but complementary aspects of coating performance: limited snow accumulation under low solar irradiance and solar-assisted ice release under stronger sunlight. Because the experiments involved different sample sets and exposure conditions, they should be interpreted as complementary demonstrations rather than as a direct quantitative comparison. S17 released the ice earlier than S12 despite the higher final surface temperature reached by S12, indicating that de-icing performance cannot be assessed from the final surface temperature alone. This suggests that interfacial ice-release behavior, together with photothermal heating, contributes to ice shedding. The persistence of de-icing capability after 50 ice push-off cycles further supports the functional durability of the coating under the conditions examined. These outdoor observations extend the assessment of coating performance to natural solar exposure, while quantitative comparisons among formulations remain based on the controlled laboratory protocols. The findings support the practical potential of combining photothermal heating with favorable ice-release properties, although longer-term exposure and repeated outdoor testing under varied environmental conditions are still required to establish service-life performance.

3.4.6. VOC content and environmental considerations

The estimated nominal VOC content ranged from approximately 370 to 417 g/L across the 18 formulations, with solvent mass fractions of 34.4–41.1 wt%. The corresponding estimates for neat PU (S2) and the optimized hybrid coating (S17) were approximately 417 and 395 g/L, respectively. Because the nominal solvent charge was fixed at 40.91 g per batch, the lower VOC concentration of S17 reflects the additional formulation volume contributed by the additives rather than reduced solvent consumption. These values provide a formulation-based estimate of the solvent content of the uncured coatings; experimental VOC determination would be required to assess compliance with applicable

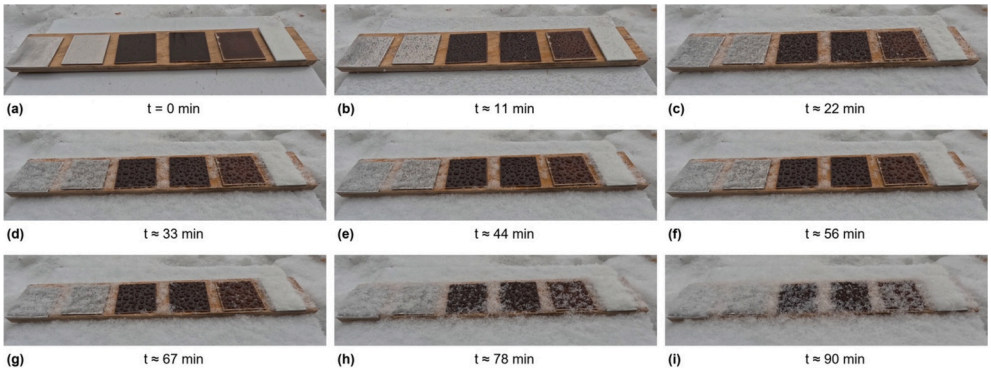


Fig. 15. Time-lapse images of snow accumulation on six surfaces during outdoor exposure at −10 °C and a light intensity of 135 ± 15 W/m^2. From left to right: bare aluminum, S2, S3, S12, S17, and a commercial coating with PU. Panels (a–i) cover approximately 90 min, with approximate elapsed time indicated beneath each image. The full recording is provided in Supplementary Video S1.

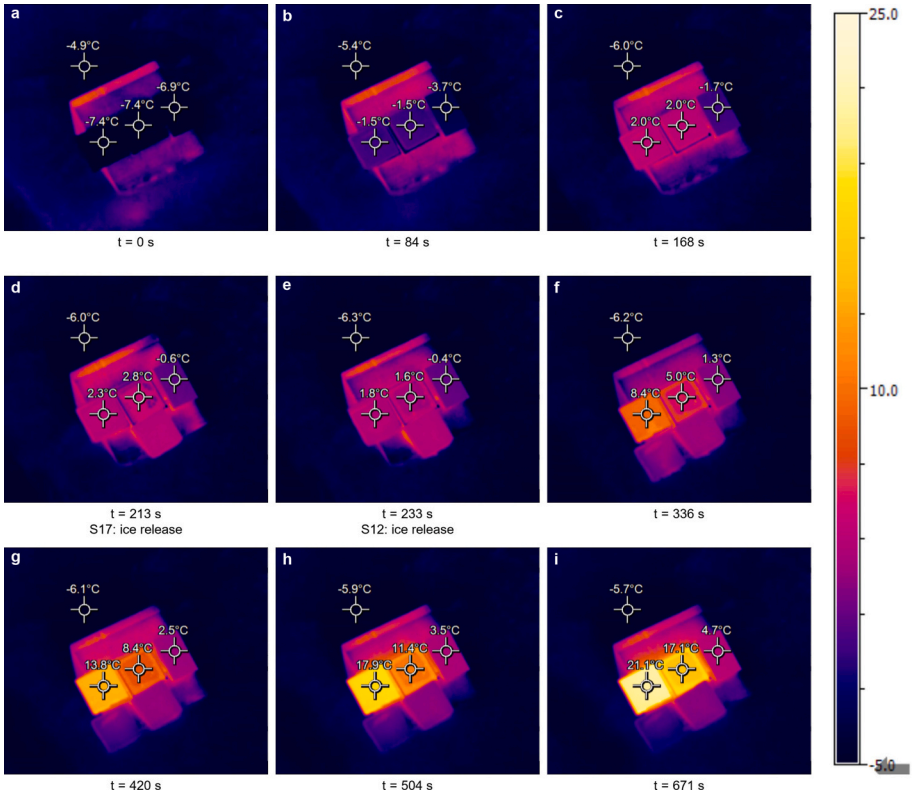


Fig. 16. Infrared thermal sequence of outdoor solar-assisted de-icing on S12 (left), S17 (centre), and a commercial white polyurethane (PU) coating (right), tested after 50 ice push-off cycles. The experiment was conducted on 4 February under a cloudless sky, with a forecast ambient air temperature of approximately −10 °C and a solar irradiance of 1043 ± 80 W/m^2. Panels (a–i) show selected stages over 671 s, including ice release from S17 at 213 s (d) and S12 at 233 s (e). Elapsed time is indicated beneath each panel. The full recording is provided in Supplementary Video S2.

regulatory limits.

The coatings retained ice-release functionality during repeated icing/deicing without coating replenishment or additional application of solvent or liquid deicers. This supports their use across successive icing events, although it does not by itself establish an environmental advantage over conventional treatments. Organic solvent use during preparation and application remains a limitation of the present system. Future work could address this limitation by reducing the solvent content or transferring the hybrid formulation to a waterborne polyurethane matrix. Such modifications should be evaluated alongside additive dispersion, film formation, water resistance, and mechanical properties to determine whether low ice adhesion and photothermal performance can be maintained. Experimental VOC characterization and, subsequently, a comparative life-cycle assessment would help establish the environmental implications of the coating approach beyond its measured anti-icing performance.

4. Conclusions

The comprehensive optimization of polyurethane-based anti-icing coatings conducted in this study has successfully established a statistically rigorous framework for overcoming the inherent dichotomy between the mechanical compliance required for low ice adhesion and the physical robustness necessary for practical deployment. Through the application of Response Surface Methodology (RSM), we have not only identified the dominant factors governing individual surface properties

but also elucidated the complex synergistic interactions that define the performance of hybrid passive/active systems. The investigation definitively confirms that the molecular topology of the amphiphilic modifier is a critical design parameter; linear PEG/PDMS copolymers (DBE—C25) exhibit a distinct advantage in migratory mobility over their graft counterparts (CMS-626), facilitating the formation of a homogeneous Quasi-Liquid Layer (QLL) that serves as the mechanism for reducing ice adhesion strength to the low regime (< 20 kPa). While the graft copolymer architecture proved more effective at suppressing ice nucleation through steric hindrance—offering a pathway for anti-frosting applications—the linear topology is superior for de-icing applications where release facilitated by interfacial slippage is paramount. Furthermore, the integration of silicone oil coated Fe_3O_4 nanoparticles introduced a dominant photothermal capability that was critical for active de-icing; however, the statistical analysis highlighted a delicate threshold where excessive nanoparticle loading (> 5 wt%) begins to reduce the polymer network's tensile strength and increase surface roughness to levels that promote mechanical interlocking with ice. The development and application of the photothermal-inclined plane test provided the empirical evidence needed to validate the synergy between these competing mechanisms, demonstrating that the optimized formulation (7.5 wt% linear copolymer, 5 wt% nanoparticles) utilizes absorbed solar energy to trigger interfacial melting while the polymeric QLL acts as a slip boundary, allowing gravity to overcome residual adhesion forces. Outdoor observations support the retention of coating functionality after repeated mechanical testing and under the outdoor conditions examined. This work shows that statistically optimized hybrid coatings can simultaneously deliver low ice adhesion (17 ± 7 kPa and IAS growth rate 0.22 kPa/cycle for S17), adequate mechanical compliance, and rapid sunlight de-icing (12 ± 3 min for 3 mm ice under 1 sun) a structurally durable, economically scalable polyurethane coating that works well in real-world icing settings can enable next-generation aerospace and wind energy protection systems.

CRediT authorship contribution statement

Mohammad Bakhtiari: Writing – review & editing, Writing – original draft, Visualization, Validation, Software, Methodology, Investigation, Formal analysis, Data curation, Conceptualization. **Gelareh Momen:** Writing – review & editing, Writing – original draft, Supervision, Resources, Project administration, Funding acquisition, Conceptualization. **Reza Jafari:** Writing – review & editing, Writing – original draft, Supervision, Resources, Project administration, Funding acquisition, Conceptualization.

Declaration of Generative AI and AI-assisted technologies in the writing process

During the preparation of this work, the authors utilized large language models (LLMs), specifically Gemini 3 by Google and QuillBot, to enhance grammatical accuracy and improve the overall readability of the manuscript. Following the use of these tools, the authors reviewed and edited the content as needed and take full responsibility for the content of the publication.

Declaration of competing interest

The authors declare that they have no known competing financial interests or personal relationships that could have appeared to influence the work reported in this paper.

Acknowledgments

The authors gratefully acknowledge the financial support provided by the Natural Sciences and Engineering Research Council of Canada (NSERC) and UQAC, for providing the necessary infrastructure to carry out this work.

Appendix A. Supplementary data

Supplementary data to this article can be found online at https://doi.org/10.1016/j.porgcoat.2026.110710.

Data availability

Data will be made available on request.

References

[1] H. Chu, et al., Eco-friendly photothermal superhydrophobic coatings: recently advances in icephobic mechanisms, efficient photothermal conversion, and sustainable anti/de-icing technologies, Adv. Colloid Interface Sci. 343 (2025) 103565.
[2] Y. Cao, W. Tan, Z. Wu, Aircraft icing: an ongoing threat to aviation safety, Aerosp Sci Technol 75 (2018) 353–385.
[3] Z. Liu, Y. Zhang, Y. Li, Superhydrophobic coating for blade surface ice-phobic properties of wind turbines: a review, Prog. Org. Coat. 187 (2024) 108145.
[4] J. Chen, et al., Experimental study on anti-icing and deicing performance of polyurethane concrete as road surface layer, Constr. Build. Mater. 161 (2018) 598–605.
[5] J. Shi, et al., Recent advances in photothermal anti−/de-icing materials, Chem. Eng. J. 481 (2024) 148265.
[6] L.T. Contreras Montoya, S. Lain, A. Ilinca, A review on the estimation of power loss due to icing in wind turbines, Energies 15 (3) (2022) 1083.
[7] M. Krapfl, Field Study Shows Icing Can Cost Wind Turbines up to 80% of Power Production, 2021.
[8] W. Li, Y. Zhan, S. Yu, Applications of superhydrophobic coatings in anti-icing: theory, mechanisms, impact factors, challenges and perspectives, Prog. Org. Coat. 152 (2021) 106117.
[9] F. Wang, et al., Dynamic anti-icing surfaces (DAIS), Adv. Sci. 8 (21) (2021) 2101163.
[10] T. Lu, et al., Flexible and scalable photothermal/electro thermal anti-icing/de-icing metamaterials for effective large-scale preparation, iScience 27 (11) (2024) 111086.
[11] X. Yin, et al., Integration of self-lubrication and near-infrared photothermogenesis for excellent anti-icing/deicing performance, Adv. Funct. Mater. 25 (27) (2015) 4237–4245.
[12] S. Chernyy, et al., Superhydrophilic polyelectrolyte brush layers with imparted anti-icing properties: effect of counter ions, ACS Appl. Mater. Interfaces 6 (9) (2014) 6487–6496.
[13] S. Wu, et al., Superhydrophobic photothermal icephobic surfaces based on candle soot, Proc. Natl. Acad. Sci. 117 (21) (2020) 11240–11246.
[14] S. Yang, et al., A critical perspective on photothermal de-icing, Adv. Mater. 37 (7) (2025) 2415237.
[15] Y. Wu, et al., Recent advancements in photothermal anti-icing/deicing materials, Chem. Eng. J. 469 (2023) 143924.
[16] Y. Li, et al., Design and long-term anti-icing mechanism of superhydrophobic TPU coatings synergistically enhanced by modified carbon nanotubes and zinc oxide, Appl. Surf. Sci. (2025) 164804.
[17] A.J. Paleo, et al., Carbon nanotube–polyurethane composite sheets for flexible thermoelectric materials, ACS Appl. Nano Mater. 6 (19) (2023) 17986–17995.
[18] H. Sojoudi, et al., Durable and scalable icephobic surfaces: similarities and distinctions from superhydrophobic surfaces, Soft Matter 12 (7) (2016) 1938–1963.
[19] M. Bakhtiari, et al., Enhancing anti-icing efficacy in hybrid polyurethane coatings: Evaluating the significance of molecular weight, chemical structure, and content of PEG/PDMS, Appl. Surf. Sci. 684 (2025) 161951.
[20] M. Bakhtiari, G. Momen, R. Jafari, Photothermal polyurethane coatings with functionalized nanoparticles and quasi-liquid layer for enhanced anti-icing and solar-assisted de-icing, Sol. Energy 300 (2025) 113859.
[21] M. Shamshiri, R. Jafari, G. Momen, Icephobic properties of aqueous self-lubricating coatings containing PEG-PDMS copolymers, Prog. Org. Coat. 161 (2021) 106466.
[22] H. Memon, J. Wang, X. Hou, Interdependence of surface roughness on icephobic performance: a review, Materials 16 (13) (2023) 4607.
[23] I.E. Kant, et al., Enhancement of the surface and mechanical properties of polyurethane coating through changing the additive ratio of silane, Adv. Mater. Interfaces 11 (11) (2024) 2300944.
[24] K. Maghsoudi, et al., Icephobicity and durability assessment of superhydrophobic surfaces: The role of surface roughness and the ice adhesion measurement technique, J. Mater. Process. Technol. 288 (2021) 116883.
[25] R. Kumar, H. Bhowmick, B. Sharma, Recent trends in icephobic polymer coatings for aerospace applications in cold climates, Polym. Adv. Technol. 36 (5) (2025) e70211.
[26] H. Liu, et al., Facile fabrication of robust and universal UV-curable polyurethane composite coatings with antibacterial properties, Polym. Eng. Sci. 63 (10) (2023) 3371–3381.
[27] K. Golovin, et al., Designing durable icephobic surfaces, Sci. Adv. 2 (3) (2016) e1501496.

[28] A. Vicente, et al., Icephobic and anticorrosion coatings deposited by electrospinning on aluminum alloys for aerospace applications, Polymers 13 (23) (2021) 4164.
[29] A. Nistal, B. Sierra-Martín, A. Fernández-Barbero, On the durability of icephobic coatings: a review, Materials 17 (1) (2023) 235.
[30] T. Lu, et al., Flexible and scalable photothermal/electro thermal anti-icing/de-icing metamaterials for effective large-scale preparation, iScience **27** (11) (2024).
[31] G. Sivakumar, S. Sundararajan, The effect of surface roughness, stiffness, and size on ice adhesion, Cold Reg. Sci. Technol. 225 (2024) 104271.
[32] F. Carreño, et al., Design and development of icephobic coatings based on sol-gel/modified polyurethane paints, Mater. Today Commun. 25 (2020) 101616.
[33] Y. Liu, et al., Sebaceous gland-inspired self-lubricated de-icing coating by continuously secreting lubricants, Prog. Org. Coat. 174 (2023) 107311.
[34] Y. Lei, et al., Mechanically robust superhydrophobic polyurethane coating for anti-icing application, Prog. Org. Coat. 183 (2023) 107795.
[35] S.G. Moghadam, G. Momen, R. Jafari, Ice-responsive coatings: evaluating the effect of hydrogen bond donors on deep eutectic solvents/ionic liquids anti-icing efficiency, J. Mol. Liq. 427 (2025) 127389.
[36] C. Liang, et al., Durable icephobic acrylic polyurethane coating with ultra-low interfacial toughness for efficient large-scale deicing, Prog. Org. Coat. 206 (2025) 109374.
[37] X. Wang, et al., A facile fabrication of durable, fluorine-free superhydrophobic cotton fabrics with integrated self-cleaning and anti-icing properties, Colloids Surf. A Physicochem. Eng. Asp. 733 (2026) 139267.
[38] J. Zhou, H. Xu, L. Tang, Facile fabrication of high performance hydrophilic anti-icing polyurethane methacrylate coatings cured via UV irradiation, Prog. Org. Coat. 182 (2023) 107657.
[39] Y. Wu, et al., Fabrication of a water repellent comb-like WPU with excellent and sustainable anti-icing performance, Appl. Surf. Sci. 680 (2025) 161412.
[40] E. Bakhshandeh, et al., New insights into tailoring physicochemical properties for optimizing the anti-icing behavior of polyurethane coatings, J. Appl. Polym. Sci. 140 (44) (2023) e54610.
[41] E. Bakhshandeh, et al., From theory to application: Innovative ice-phobic polyurethane coatings by studying material parameters, mechanical insights, and additives, Surf. Interfaces 51 (2024) 104545.
[42] Y. Du, et al., A crosslinked silicone coating adjusted by an additive with promising antifouling and ice nucleation inhibition performance, New J. Chem. 48 (2) (2024) 693–702.
[43] T. Bharathidasan, et al., Effect of wettability and surface roughness on ice-adhesion strength of hydrophilic, hydrophobic and superhydrophobic surfaces, Appl. Surf. Sci. 314 (2014) 241–250.
[44] Y. Gao, et al., Solvent-free bottlebrush elastomer coatings with controllable architecture via one-step photopolymerization: Ultra-low ice adhesion and durable icephobicity, Prog. Org. Coat. 210 (2026) 109696.
[45] Z. He, et al., Design and preparation of icephobic PDMS-based coatings by introducing an aqueous lubricating layer and macro-crack initiators at the ice-substrate interface, Prog. Org. Coat. 147 (2020) 105737.
[46] Z. Lingru, et al., PDMS and POSS-dangling zwitterionic polyurethane coatings with enhanced anti-icing performance, Prog. Org. Coat. 170 (2022) 106972.
[47] T. Wang, et al., Mechanism and design strategy of ice-phobic surface: a comprehensive review, Adv. Colloid Interface Sci. 341 (2025) 103478.